UNIVERSITY OF CALIFORNIA SAN DIEGO

The Influence of Meteorology and Cloud Properties on Downwelling Shortwave and Longwave Irradiance at Ross Island, Antarctica

A Thesis submitted in partial satisfaction of the requirements
for the degree Master of Science

in

Earth Sciences

by

Kristopher Scarci

Committee in Charge:

Dan Lubin, Chair
Joel Norris
Lynn Russell

2018

The thesis of Kristopher Scarci is approved, and it is acceptable in the quality and form for publication on microfilm and electronically:

_____

_____

_____

Chair

University of California San Diego

2018

TABLE OF CONTENTS

LIST OF FIGURES

LIST OF ACRONYMS

AAO	Antarctic Oscillation
ACC	Antarctic Circumpolar Current
AMF	ARM Mobile Facility
AMF2	Second ARM Mobile Facility
ARM	Atmospheric Radiation Measurement
ARSCL	Active Remote Sensing of Clouds
AT	Atmospheric Transmission
AWARE	ARM West Antarctic Radiation Experiment
AWS	Automatic Weather Station
BB	Broadband
BWCJ	Barrier Wind Corner Jet
EA	East Antarctica
EAIS	East Antarctica Ice Sheet
CCN	Cloud Condensation Nuclei
CEIL	Ceilometer
CRE	Cloud Radiative Effect
DJF	December, January, February
DOE	U.S. Department of Energy
ENSO	El Niño Southern Oscillation
ERA	European Reanalysis
ESDC	Earth Sun Distance Correction
FCC	Fractional Cloud Cover
GMT	Greenwich Mean Time
GPM	Geopotential Meters
HP	High Pressure
INTERPSONDE	Interpolated Balloon-Borne Sounding System
IR	Infrared
ISO	International Organization for Standardization
KAZR	Ka-band ARM Zenith Radar
LP	Low Pressure
LW	Longwave Radiation
LWP	Liquid Water Path
MATLAB	Matrix Laboratory
MCM	McMurdo Station, Antarctica
MFR	Multifilter Radiometer
MFRSR	Multifilter Rotating Shadowband Radiometer
MPL	Micropulse Lidar
NaN	Not a Number
NB	Narrowband
NSF	U.S. National Science Foundation
PGF	Pressure Gradient Force
PI	Principal Investigator

PLR	NSF Division of Polar Programs
QC	Quality Control
RAS	Ross Ice Shelf Air Stream
RIS	Ross Ice Shelf
SAM	Southern Annular Mode
SH	Southern Hemisphere
SKYRAD	Sky Radiometers on Stand for Downwelling Radiation
SIO	Scripps Institution of Oceanography
SLP	Sea Level Pressure
SONDE	Balloon-Borne Sounding System
SRB	Surface Radiation Balance
SW	Shortwave Radiation
SZA	Solar Zenith Angle
T2M	Temperature at 2 meters
TAM	Transantarctic Mountains
TCC	Total Percentage Cloud Cover
TRC	Raw Cloud Transmittance
TSI	Total Sky Imager
UCSD	University of California, San Diego
USAP	U.S. Antarctic Program
UTC	Coordinated Universal Time
VAP	Value Added Product
WA	WA
WAIS	West Antarctic Ice Sheet
Z700	Geopotential Height of 700 hPa Pressure Level

ACKNOWLEDGMENTS

I'd like to thank my adviser, Dr. Dan Lubin, for his guidance as I pursued my MS in Climate Science. Dan is an adept research physicist, and mindfully approached my development as a researcher by fostering a sense of scientific inquisitiveness, while mapping out proper approaches when conducting rigorous research. Dan was extremely generous with his time, always willing to address my questions – no matter how basic or trivial. I am extremely appreciative of his mentorship and attention-to-detail while overseeing my MS thesis work while at SIO.

I'd also like to the thank PhD Candidate Ryan Scott. Ryan was instrumental throughout my entire process as a MS candidate, acting as an effective science communicator, math aficionado, and programming tutor – all while treating me as a peer. His passion for his work is contagious, and served to motivate me throughout the research process. He also appreciates great music! I wish him the best as he graduates SIO in the summer.

This thesis in part is currently being prepared for submission for publication in a peer-reviewed journal, with coauthors Scarci, Kris; Scott, Ryan; and Lubin, Dan. The thesis author was the primary investigator and author of this material.

ABSTRACT OF THE THESIS

The Influence of Meteorology and Cloud Properties on Downwelling Shortwave and Longwave Irradiance at Ross Island, Antarctica

by

Kristopher Scarci

Master of Science in Earth Sciences

University of California San Diego, 2018

Dr. Dan Lubin, Chair

ABSTRACT

Understanding the effect of clouds on atmospheric radiative processes affecting downwelling radiation is critical in discerning the causal nature of large-scale melt events in Antarctica. The influence of varying cloud types on solar and terrestrial radiation presents itself as a multifarious problem interwoven within many hierarchical orders of physical interactions across a range of spatial scales. In this work we show how large-scale meteorology leads to advection of moisture over varying terrain, influencing the microphysical properties of clouds and their effect on shortwave and longwave radiation at the Antarctic surface.

Synoptic circulation patterns over West Antarctica (WA) were grouped and categorized by Scott et al. 2018 into four recurring meteorological regimes using *k*-means cluster analysis of daily 700 hPa geopotential height fields. Regime 1 is representative of warm surface air temperature, and moist marine air advection over WA with liquid-bearing and classical liquid-dominated mixed-phase clouds. Regime 2 is characterized by large-scale subsidence, outflow of continental polar air, and anomalously clear skies. Regime 3 is of smaller sample size, and produces similar surface radiative flux levels to those of Regime 1. Regime 4 is distinguished by an orographic influence upstream of Ross Island, resulting in the formation of geometrically thick, mixed-phase clouds.

This study focuses on the radiative differences in downwelling shortwave and longwave irradiance by comparing prevailing meteorological regimes and cloud properties therein. The influence of supplemental ice absorption on downwelling shortwave flux is highlighted when comparing cloud optical depth properties of Regime 4 to that of Regime 1 and 2. The influence of cloud base temperature on downwelling longwave flux is noted when comparing cloud optical depth properties of Regime 2 to that of Regime 1.

Section 1

Introduction

1.1 AWARE Campaign

As one of the fastest warming regions on the planet, West Antarctica (WA) is a critical region within the global climate system. WA's vulnerability to ice melt induced by warm weather events during the Antarctic summer months (DJF) requires understanding of the meteorological regimes and associated cloud systems that dominate over WA. The US Department of Energy's (DOE) Atmospheric Radiation Measurement (ARM) program recognized this need for greater scientific understanding of this critical geographic region of climatic importance. ARM worked in tandem with the National Science Foundation (NSF) to support and deploy the ARM West Antarctic Radiation Experiment (AWARE) research campaign, which was dedicated to the study of the pristine atmosphere overlying WA (Lubin et al., 2015).

Perennial cyclonic weather systems persist off the coasts of the Antarctic continent. Antarctic meteorology differs largely from that of the Arctic due to the contiguous forcing of diverse Antarctic terrain, particularly evident in the asymmetric landscape of WA. In contrast to the Arctic, relatively little is known regarding the cloud radiative forcing and microphysical properties of Antarctic cloud systems (Bromwich et al., 2012); (Scott and Lubin, 2016). This dearth of information provided the major motivation for the AWARE campaign.

Based at McMurdo Station, Ross Island, from November 2015 to January 2017, and at the WAIS Divide Ice Camp between December 2015 and January 2016 – the AWARE campaign comprised the first rigorous atmospheric and climatological research in WA in over 50 years, with the last substantial field work being conducted in the 1957 International Geophysical Year. Data acquisition during the intermediary period between 1957 and present-day was limited to satellite imagery, reanalysis data, and Automatic Weather Station (AWS) data. A closer look at these datasets indicated the susceptibility of WA to warming via advection of maritime-originating heat and moisture transport. In order to gain greater insight into the underlying physical mechanisms, more robust datasets would be required to ascertain characteristics behind the atmospheric thermodynamics, dynamics, moisture transport, cloud properties, and energy balance. Particular emphasis is placed on the cloud radiative effect (CRE) on surface radiation balance (SRB), as cloud information at high latitudes in the southern hemisphere is limited (Scott et al. 2017).

The AWARE Campaign deployed a wide range of advanced radiometric, meteorological, and remote sensing instruments to McMurdo Station. Based on the southern tip of Ross Island, McMurdo Station, the hub of the United States Antarctic Program (USAP) was the home-base for the Second ARM Mobile Facility (AMF2) that provided the major instrument suite for the AWARE campaign. This location is adjacent to the northwestern Ross Ice Shelf (RIS), Victoria Land, the Transantarctic Mountains (TAM), and the Ross Sea. Ross Island experiences similar meteorology patterns to much of WA, and data acquired at AMF2 provides an excellent analog for comparison. Key physical processes underlying the surface radiation budget (SRB), synoptic and mesoscale meteorology, cloud radiative effect (CRE), cloud microphysical properties, and orographically induced cloud dynamics will continue to be explored and analyzed using the data acquired by

AWARE for years to come. Available on the ARM website, AWARE's extensive data archive will provide lasting value to the scientific community (Lubin et al., 2015).

The AMF2 instruments provided a breadth of data, enabling researchers to better model underlying physical mechanisms regarding downwelling and upwelling shortwave and longwave irradiance, total cloud fraction, cloud geometry, cloud phase, optical depth, cloud base temperature, and meteorological circulation trends. Elucidating relationships between cloud characteristics, meteorology, and downwelling radiation is our main objective in this work, as changes in cloud radiative processes can lead to cryospheric melt during the summer season (Nicolas et al., 2017). Regions of interest include the RIS, the West Antarctic Ice Sheet (WAIS), the Antarctic Peninsula; of particular interest to this study, Ross Island experiences meteorological conditions relevant to these regions, and is thus explored as a spatial reference for comparison.

Equally important to the climate impact, understanding the role of regional topography and meteorology on cloud-formational processes is crucial in improving the reliability of McMurdo Station weather forecasts. The summer season at Ross Island is the busiest time of year in terms of local flight operations, and the tight logistical schedules pose ever-present risks. Improving simulations of Antarctic clouds and meteorology are a necessity for safer operations at McMurdo Station (Scott and Lubin, 2014).

1.2 Area of Study

The cold, pristine conditions of the Antarctic atmosphere remain relatively unperturbed by anthropogenic aerosol forcing. As the largest reservoir of ice on the planet, Antarctica is geographically bifurcated into WA and Eastern Antarctica (EA). Acting as this divisional boundary, the Transantarctic Mountains (TAM) extend ~3500 km from Victoria Land to Coats Land, providing a southern boundary to the Ross Ice Shelf (RIS). Dividing the Amundsen Sea to the east and Weddell Sea to the west, the Antarctic Peninsula is another geographic feature of climatic importance. The Antarctic Peninsula juts outward from Palmer Land and extending past the Antarctic Circle towards the tip of South America, and hence influences the path of the highly dynamic Southern Ocean storm tracks.

Key differences between WA and EA are most evident in the asymmetrical terrain of WA, when compared to the relative homogeneity of dome-shaped EA. Smaller in landmass and at considerably lower average elevation – which plays a significant role in sensitivity to warmer temperatures – WA provides a large volume of freshwater storage in the form of ice sheets, ice shelves, ice streams, and fast-moving glaciers that flow down-slope towards the Southern Ocean. Situated at low-lying elevations, important features of WA – such as WAIS and RIS – are exposed to marine-air injection and oceanic heat exchange (Nicolas and Bromwich 2011). The high and gently sloping terrain of EA vastly differs from the nuanced WA terrain in that the coastal boundaries of EA are fortified with elevated slopes, acting as a natural barrier to marine airmass perturbations (Lubin et al., 2015). This results in large-scale subsidence on the larger East Antarctic Ice Sheet (EAIS), leading to colder temperatures, drier conditions, and minimal cloud generation (Scott and Lubin, 2014). Physical and meteorological properties of EAIS provide a stark contrast to that of WAIS, as the EAIS demonstrates both thermodynamic and dynamic

stability resulting in a yearly net-gain of ice-mass (Shepherd et al., 2012); (Zwally et al., 2015); whereas WAIS is experiencing land-ice loss at a growing annual rate, contributing to global sea level rise (Shepherd et al., 2012); (Kopp et al., 2016).

Ross Island itself is of volcanic origin, and is situated at the northwestern edge of the RIS. Established on Ross Island in 1956, McMurdo Station is a maritime site located at 77.85°S, 166.66°E. Due to its close proximity to the Ross Sea, Ross Island experiences many ocean-bourne frontal systems and low-lying clouds, which are linked to lack of sea-ice cover (Scott and Lubin, 2016). Ross Island is also exposed to southerly winds originating for the Antarctic interior via a clockwise quasi-geostrophic cyclone over the Ross and Amundsen Seas, causing moist marine-air to be advected over WAIS towards the TAM over the southern portion of the RIS (Nicolas and Bromwich, 2011). Seasonal temperatures at Ross Island remain below freezing year round (Monaghan et al., 2005).

Section 2

Site Representativeness

2.1 Cloud Radiative Effect

Understanding the influence of clouds on downwelling radiation, thermodynamics, and atmospheric dynamics is critical for complete understanding of interdependent systems, involving a wide array of multivariate forcings and feedbacks. Improving our understanding of the cloud radiative effect (CRE) in both the shortwave and longwave will ultimately enhance the ability to model and predict changes to the planet's cryosphere. Current models and simulations inadequately model cloud patterns over WA, thus creating the need for improved radiative transfer models and representations of meteorological regimes that govern cloud formation, and subsequent effects on the SRB (Bromwich et al., 2012); (Scott et al., 2017).

The goal of this study is to develop an empirical relationship between Antarctic summer (DJF) cloud-systems and downwelling shortwave/longwave radiation over Ross Island, and discover connections between cloud properties as a function of prevailing meteorological circulation patterns (Scott and Lubin, 2014). Using data acquired during the AWARE campaign, this study attempts to establish partial groundwork in the “flux-cloud-meteorology” relationship by analyzing downwelling radiation over Ross Island and by developing correlations between summer cloud-system properties and recurring meteorological regimes.

2.2 Examples of Data

Daily cloud cases of 10DEC2015 (Figure 1a) and 11JAN2016 (Figure 1b) are presented to demonstrate the generalized influence of clouds on surface radiation. Over the course of 24 hours, the cloud cover on 10DEC2015 (Solar Noon ~0100Z) transitions from overcast (0000-0400Z) to clear-sky (0400-1700Z) to fractional cover (1700-0000Z). These cloud coverage transitions are marked by fluctuations in both shortwave and longwave radiation. In the morning, downwelling shortwave is perturbed due to cloud-edge effects, while the longwave is boosted by approximately 20 W m^{-2} due to the presence of overcast clouds. As clear-sky conditions prevail in the afternoon, longwave flux drops to a baseline level for summer clear-sky conditions (~220 W m^{-2}), while the shortwave exhibits a smooth curve as it follows the changing solar zenith angle. As fractional cloud cover emerges in the evening, the downwelling longwave signature nearly traces the total cloud cover cover time-series plot, exhibiting a strong cloud/longwave correlation. The case of 11JAN2016 differs from 10DEC2015 by being subject to total overcast for the majority of 24 hours, resulting in significantly smaller downwelling shortwave flux (as large as 400 W m^{-2} in attenuation) and greater downwelling longwave flux (as large as 70 W m^{-2}) when compared to the fractional and clear-sky intervals of 10DEC2015.

2.3 AWS Stations

Automatic Weather Station (AWS; Lazzara 2010) surface air temperature data were used to demonstrate whether conditions at Ross Island are representative of other WA regions. Although distant from most of WA, Ross Island is geographically positioned so as to be relevant to other locations that harbor large ice masses susceptible to melt. Approximately one decade of

surface air temperature data (2007 – 2016) was acquired from multiple AWS stations across WA and the RIS. AWS data were downloaded from the UW-Madison's Space Science & Engineering Center's website "Antarctic Meteorological Research Center & Automatic Weather Stations Project." The following AWS are represented in this study: Willie Field, Cape Bird, Windless Bight, Linda, Lorne, Ferrell, Emilia, Margaret, Minna Bluff, Byrd, Kominko-Slade, Siple Dome, Dismal Island, and Evans Knoll, with Evans Knoll being the sole AWS station without a full decadal dataset (2011 – 2016). The map in Figure 2 displays the locations of each station used in this study (enclosed in green rectangles).

Figure 3 presents boxplots for each of these AWS, and show how summer temperature averages vary spatially across the greater region of interest. Willie Field is one of the airstrips serving Ross Island, and represents the closest location to McMurdo Station. A dashed-cyan line extends from Willie Field's median decadal surface temperature (-5.98°C), and provides a visual reference for comparison to other AWS stations (ordered by proximity to Willie Field). As expected, AWS stations situated on the elevated interior of WAIS (Byrd and Kominko-Slade) trend towards colder than average surface temperatures. Also located on WAIS but situated to the west on lower terrain, Siple Dome resides near the boundary of WAIS and the eastern RIS, and thus experiences warmer average temperatures than its elevated counterparts at Byrd and Kominko-Slade (WAIS Divide). Siple Dome is in close vicinity to a recent large-scale WAIS melt event that occurred in January of 2016 (Nicolas et al., 2017). The Siple Coast confluence zone consists of marine-air injected over WAIS and katabatic winds occurring as westward moving airmasses descend towards RIS. A similar temperature regime to that of Willie Field persists at the spatially distant Evans Knoll (Pine Island/Thwaites Glaciers) residing in the Amundsen Sea embayment. Situated at relatively lower latitude on the Antarctic Peninsula, Dismal Island (proximal to the

Larsen Ice Shelves) is characterized by the warmest average temperature (it is the sole AWS station considered here with an average temperature above freezing). Residing on the western RIS are Emilia, Linda, Lorne, and Ferrell. The closest AWS stations to McMurdo Station (Willie Field) are Cape Bird and Windless Bight.

AWS data were also used to corroborate the *k*-means regime clustering algorithm (detailed in Section 3), which groups synoptic weather regimes over WA into four major classifications of synoptic meteorology influencing Ross Island. Once a 10 year surface temperature average was calculated for each AWS station, daily temperature anomalies were computed by subtracting the 10 year average from the mean of each day's surface temperature. This process was conducted for each summer month separately – i.e. the 10 year average of surface temperatures for the month of December was subtracted from each and every December date. The same was done for January and February. Upon computing the temperature anomaly value for each day, the daily values were sorted into regimes based on the k-means clustering results. Averages were then computed using the constituent days within each regime, resulting in a total of four average surface temperature values (one per regime) for each AWS station, signifying each regime's decadally averaged temperature anomaly. Sorted into meteorological regimes, surface temperature anomalies were used to corroborate findings from Ryan Scott's ERA-Interim Reanalysis T2M (Figure 5) composite (Scott et al., 2018).

Regime 1 showcases the warmest surface air temperatures with particular intensity over Marie Byrd Land, while Regime 2 shows the coldest surface air temperatures of all regimes. Regime 3 is another warm regime with most anomalous temperatures over Victoria Land and the Antarctic Peninsula. Regime 4 represents the orographic regime that impacts RIS and Ross Island, and is marked by a slight warm anomaly over RIS and Ross Island.

Section 3

Methodology

3.1 *k*-means Clustering Algorithm

The *k*-means clustering method was used in this study to categorize the AWARE data into regimes of similar recurring synoptic meteorological conditions. Developed in Scott et al. 2018, this method uses a collection of decadal (2007-2016) ERA-Interim Reanalysis data to decipher numerically-similar trends within ~10,000 700-hPa geopotential height field samples (Figure 4). Decadal means and distributions of daily anomalies were then calculated for WA, to serve as inputs to the *k*-means clustering algorithm (Scott et al., 2018).

The *k*-means clustering algorithm functions as a "smart sorting" procedure that sorts data into groups based on similar statistical trends. The algorithm allows a user to partition a initial dataset – prior to any sort of initial analysis – into naturally forming groups of numerical distributions (Johnson and Feldstein, 2010). Setting the "*k*" value allows the user to determine the final number of sorted clusters; or in the case of this study, "regimes". The determination to set k = 4 was chosen though experimentation and by analyzing the final sorted clusters – noting the distributional characteristics within each cluster, and if said characteristics were worthy of distinction.

Upon execution, the *k*-means algorithm iteratively sorts each data point based on similarities and refines each cluster after every repetition. During each pass, every data point is compared to the local cluster's centroid, which is a collection of stored feature-values that define the likeness of each cluster. The total number of centroids is determined by the aforementioned *k*-value. Data points are assigned to the closest Euclidean centroid as the k-means program executes. Centroid assignment is determined by the lowest squared distance value. Through continuous iterations, centroids are recomputed by taking the mean of all assigned data points, reducing the variance with each pass. This recursive process is repeated until no data point changes the centroid assignments, resulting in the finalized clusters. We note that the *k*-means algorithm is sensitive to the initial arrangements of centroids when beginning the clustering procedure (Trevino 2016).

Using the results from the *k*-means outputs (Figure 6), each regime distribution can be analyzed based on numerical characteristics and statistical trends, and then correlated with particular research data not involved in determining the regimes. AWARE datasets can thus be temporally sorted using this schema, providing a way to interpret ground-based measurements in terms of each regime's unique synoptic properties.

3.2 Regime Classifications

Each regime offers unique characteristics and meteorological patterns that provide insight into major synoptic circulations that dominate over WA. Ross Island experiences both northerly onshore flow and southerly moisture transport. It's unique geographic positioning confines it to a corridor of periodic southerly winds by way of the onshore flow over the WAIS

and RIS. At the western RIS, airmasses are then exposed to strong katabatic flow through glacial valleys. Combined with barrier winds trapped at the base of the TAM, a confluence zone of southerly moving wind becomes manifest (Parish et al., 2006).

Using Figures 4 and 5 as references, Regime 1 (23 days) is characterized by high pressure ridging over the Amundsen Sea and a weakened low pressure trough over the Ross Sea. This meteorological scenario leads to moist marine air being advected over WAIS and the RIS towards Ross Island, resulting in mainly liquid-phase clouds. The warmest surface air temperatures are represented by days within this regime, with particular intensity over Marie Byrd Land. The Ross Sea is prone to common cyclonic disturbances, producing complex frontal systems. The liquid-water dominated cloud systems of Regime 1 indicate characteristics of maritime onshore flow by way of the Ross Sea. This marine-air injection is marked by shallow boundary layer clouds (Scott and Lubin, 2014).

Regime 2 (31 days) is characterized by high pressure ridging over the Ross Sea and a low pressure trough over the Bellinghausen Sea. This geopotential arrangement favors large-scale subsidence, outflow of continental polar air, and anomalously clear skies. The coldest surface air temperatures of all regimes – along with lowest cloud fraction – are represented by this regime distribution.

Regime 3 (8 days) is characterized by a crescent-shaped high pressure ridge at 700 hPa covering the majority of WA, along with a weak low pressure area in the northern Amundsen Sea. Producing similar surface radiative flux levels to those of Regime 1, the majority of Regime 3 days are indicative of a single weather system. Of the 8 days that comprise Regime 3, only half of the days possess significant cloud fraction (30DEC2015 – 02JAN2016). Due to the lower sample size of Regime 3, it is excluded from much of the analysis in this study. Regime 1 and Regime 3 do not

occur during February 2016.

Regime 4 (29 days) is characterized by a large low pressure trough over the Ross Sea. The cyclonic nature of this regime's geopotential arrangement is indicative of marine air intrusion over central WA, followed by southerly outflow over the RIS and Ross Island. The western boundary of RIS shows signs of complex atmospheric dynamics such as vortices and low-level jets, generated by an orographic influence at the TAM. Residing on the leading edge of the low pressure cyclone, Ross Island experiences the effects of orographically lifted cloud systems, which tend to be radiatively dominated by the ice phase, due to the rapid uplifting of airmass due to the terrain (Scott et al., 2017). The Amundsen Sea acts as the primary source of cumulative moisture (Tsukernik and Lynch, 2013). Clouds over Ross Island associated with Regime 4 are observed at greatest geometrical thickness during the summer months. The cloud ice water content (IWC) associated with Regime 4 tends to be most plentiful within the cold mixed-phase temperature range of $-40°C < T < -20°C$. The influence of IWC is also most strongly apparent during summer months (Scott and Lubin, 2016).

Enhanced IWC observed in Regime 4 is consistent with modeled IWC fields and reanalyzed precipitation fields of the western RIS (Fogt and Bromwich, 2008). The orographic influence on Regime 4 IWC is also corroborated by satellite evidence using zonal transects of Cloudsat/CALIPSO cloud fraction analysis along 81°S (Bromwich et al., 2012). A study done by (Steinhoff et al., 2009) demonstrates the link between low-level convergence at the TAM boundary, resulting in strong vertical induced motion to support mixed-phase cloud formation. The low-level converging air masses are strengthened by marine-air advection by way of WAIS. This orographic lifting of a moist airmass provides an essential mechanism for ice nucleation in mixed-phase clouds (Scott and Lubin, 2016).

3.3 Regime 4 & the Ross Ice Shelf Airstream (RAS)

As a meteorological feature unique to the Ross Ice Shelf (RIS), the RIS Air Stream (RAS) is a dominant wind regime generated by airmasses interacting with unique regional topography. Combined with synoptic and mesoscale circulation patterns, such as the semi-permanent cyclone off the coast of Marie Byrd Land, the unique arrangement of terrain and cryosphere results in the formations of katabatic and barrier winds which combine in lower-lying confluence zones to form the RAS (Parish et al., 2006).

Resulting from large-scale confluent flow, katabatic winds form when negatively-buoyant air flows over downward sloping terrain, advecting cold continental air towards northern maritime situated geography. The TAM provide the genesis point for much of the sinking action of katabatic winds, as airflow is guided downward through glacial valleys, spilling onto the RIS and forced northward via the Coriolis effect. (Nigro and Cassano, 2014).

Acting as a barrier to atmospheric flow, the TAM plays a significant role in the formation of another terrain induced air-flow feature referred to as “barrier winds”. Barrier winds form parallel to the TAM when stably stratified fluid follows toward a topographic barrier. Due to the height and size of the mountainous features the TAM, the stratified flow can be partially impeded if it does not possess the sufficient kinetic energy to cross the terrain boundary. Cold air pooling causes a buildup of airmass near the surface, leading to an outward pressure gradient force (PGF) away from the TAM. Increased pressure at the base of the air column creates a PGF away from the topographic barrier. The Coriolis force (acting to the left in SH) then establishes a barrier-parallel flow that is in near geostrophic balance, resulting in mean southerly flow at the base of the air column. Barrier winds flow southerly along the mountainous boundary and often exceed the height of the TAM (~3000m) (Nigro and Cassano, 2014).

As these low-level barrier winds reach the terminus in the topography (that same barrier topography that catalyzed the formation of the barrier winds) high pressure air converges with the region's background pressure field, aligning with the local PGF leading to a magnification in local wind speed. The resulting wind pattern is a specific type of barrier winds known as “barrier wind corner jets (BWCJ)” (Nigro and Cassano, 2014).

The southerly flow of the RAS over the RIS and northward to the Southern Ocean plays a significant role by functioning as an integral component of tropospheric flow in the Southern Hemisphere. The RAS catalyzes the equator-ward transport of energy and airmass via the Siple Coast confluence zone, and is noted to be slightly weaker during Antarctic summer months (DJF) due to the weaker temperature inversion due to surface emission exceeding atmospheric emission (Steinhoff et al., 2009).

3.4 Instruments

The Total Sky Imager (TSI) provides hemispheric sky coverage measurements during daylight hours to record the daily cloud fraction as a function of time. Designed to operate at solar elevation angles greater than 10°, the TSI algorithm splits the cloud fraction measurements into two main variables: *percent_opaque* and *percent_thin*. These variables can then be summed to create a *total_percent_cloud_cover* variable (values range from 0-100%). Our study used an overcast classification threshold of ≥ 95% total percent cloud cover. The TSI dataset also includes photographic and video imagery to go along with the raw numerical data. This imagery is processed when the solar elevation angle is greater than 3° (Long et al., 2001).

The Sky Radiometers on Stand for Downwelling Radiation (SKYRAD) radiometer suite

provides continuous measurements of downwelling hemispheric broadband irradiance. SKYRAD measures both downwelling shortwave and longwave irradiance. The SKYRAD instrumentation includes both an upward-facing precision spectral pyranometer and an upward-facing infrared radiometer, designed to receive downwelling shortwave irradiance and downwelling longwave irradiance respectively (Coulson 1975). The SKYRAD variables used in this study are *down_short_hemisp* and *down_long_hemisp1*, signifying downwelling shortwave and downwelling longwave respectively, in $W\ m^{-2}$. All broadband measurements are calibrated to provide radiation for the full spectrum, with a value of 1361 $W\ m^{-2}$ being used for the solar constant. The PSP model radiometer – used to measure downwelling shortwave in the SKYRAD instrumentation suite – has a responsivity of 9.0 $\mu V/(W\ m^{-2})$, and a measurement calibration uncertainty of ±4.0% to -(4% + 20 $W\ m^{-2}$) when the solar zenith angle < 80°. The PIR model radiometer – used to measure downwelling longwave in the SKYRAD instrumentation suite – has a responsivity of 4.0 $\mu V/W\ m^{-2}$, and a measurement calibration uncertainty of ±(5.0% + 4 $W\ m^{-2}$) when the solar zenith angle < 80°. Samples from SKYRAD are recorded at a time interval of 60 seconds (Andreas 1996).

Our study uses SKYRAD shortwave irradiance data for multiple purposes, to include: estimating broadband atmospheric transmission, by taking a ratio of the measured downwelling shortwave irradiance to the solar constant multiplied by the cosine of the solar zenith angle and Earth-Sun distance correction. SKYRAD shortwave irradiance measurements are also used when calculating daily-averaged broadband albedo. SKYRAD longwave irradiance data are interpreted directly using the cloud properties derived from other instruments and the four meteorological regimes.

As the downward-facing equivalent of SKYRAD, “Ground Radiometers on Stand for

Upwelling Radiation (GNDRAD)" is used to measure upwelling shortwave and longwave irradiance. The GNDRAD instrumentation suite detects surface-reflected shortwave irradiance in and surface-emitted longwave (terrestrial) irradiance. GNDRAD shortwave values are used in conjunction with corresponding SKYRAD shortwave values (daily GNDRAD divided by daily SKYRAD) to derive the daily-averaged surface reflectance or albedo. These albedo calculations later serve as inputs in cloud optical depth calculations. Using the same model radiometers (carrying with them the same responsivity values) as SKYRAD to measure shortwave and longwave respectively; the GNDRAD PSP radiometer has a calibration measurement uncertainty of ± 2.0% or 10 W m^{-2}, and the GNDRAD PIR radiometer has a calibration measurement uncertainty of ± 2.0% or 2 W m^{-2}.

Atmospheric temperature vertical profile data are provided via the balloon-borne sounding system (SONDE). These in situ instruments vertically profile the local air during ascent through the atmosphere, providing measurements on the ambient thermodynamics, humidity, and wind characteristics. At M1 (McMurdo), soundings were typically launched twice per day – once in the afternoon and once in the evening (Sivaraman et al., 1994).

The Active Remote Sensing of Cloud Locations (ARSCL) data product is an ARM-Program value added product (VAP) that integrates multiple datasets to provide accurate estimates of various atmosphere and cloud properties. The ARSCL VAP merges data from a variety of specific instruments, to include: KAZR (Ka-band ARM Zenith Radar), MPL (Micropulse Lidar), CEIL (Ceilometer), SONDE (Balloon-Borne Sounding System), and MWR (Microwave Radiometer) (Clothiaux et al., 2001).

Variables extracted from the ARSCL dataset include *cloud_layer_top_height* and *cloud_layer_base_height*. These variables are produced via a combination of radar and lidar

measurements, and are divided into a maximum 10 potential hydrometeor layers. Data analysis conducted using these variables provides insight into cloud geometry – such as base height, top height, thickness, and number of layers – and can be used in tandem with another VAP dataset "INTERPSONDE" to accurately pinpoint cloud base temperatures.

The Interpolated Sounding (INTERPSONDE) VAP uses sounding data from the balloon-borne sounding instrument SONDE to generate a data grid with fixed time-height attributes, providing a time resolution of 1 minute for 332 levels (surface to 40 km). Typically, SONDE data are acquired twice daily during afternoon and evening launches. The INTERPSONDE VAP then uses the SONDE data as inputs to create a continuous gridded data approximation for the entire day at each height level. Variables such as air temperature, pressure, and wind speed are examples of data represented by INTERPSONDE. The time resolution of INTERPSONDE is especially useful when approximating cloud base temperatures throughout the day, as cloud base heights fluctuate as a function of time (Jensen et al., 2016).

The Multifilter Rotating Shadowband Radiometer (MFRSR) passively measures selected narrowband channels in the shortwave portion of the electromagnetic spectrum. The nominal wavelengths of the included channels are 415, 500, 615, 673, 870, and 940 nm. The MFRSR instrument combines four sets of measurements to form a single complete data record. This is executed by sampling downwelling irradiance during four distinct shadowband positions: nadir, first side-band, sun-blocked, and second side-band (Harrison and Michalsky, 1994).

Our study uses the 870 nm MFRSR channel due to the atmospheric transparency in this wavelength range. This narrowband channel is also the reference wavelength in MFRSR aerosol optical depth retrievals. The specific variable used from the MFRSR dataset is *hemisp_narrowband_filter5*, which provides downwelling irradiance values in the spectral range

of 870 nm in units of W m^{-2}. This narrowband hemispheric irradiance variable is offset-subtracted and cosine-corrected. This variable is used in calculations involving narrowband albedo, narrowband atmospheric transmission, and narrowband optical depth (Ermold et al., 1990).

The Multifilter Radiometer (MFR) is the downward facing equivalent of the MFRSR instrument. Mounted on a tower pointing toward the surface, the MFR measures upwelling narrowband irradiance in the same channels as the MFRSR (Mendoza et al., 1990). By taking a ratio of the upwelling irradiance of a specific MFR channel to the downwelling MFRSR irradiance on same wavelength channel, an accurate narrowband albedo can be computed. Our study takes a ratio of MFR to MFRSR to acquire a narrowband albedo at the 870nm wavelength. Both the MFR and MFRSR have an instrument uncertainty of 0.06% per 250 mV, resulting in an accuracy of 0.15 mV.

3.5 Example Days from Each Regime

Figure 7 shows a collection of radar (KAZR) and lidar (MPL) plots representing a selected day from each meteorological regime. The KAZR provide measures of radar reflectivity (dBz), mean doppler velocity (m/s), and spectral width (m/s); while the MPL provides displays of co-polarized backscatter and depolarization ratio.

22DEC2015 from Regime 1 is characterized by geometrically thin, liquid water clouds transported via northerly onshore flow from the Ross Sea. A low-level liquid water band is indicated by the low lidar depolarization ratio and large backscatter signature due to liquid water strongly attenuating lidar. The rightward-slant is close in characteristic to summer clouds

observed in the Arctic (Shupe et al., 2006). The resulting cloud-radiative behavior is near-blackbody in the longwave, with an average downwelling longwave measurement of 280 W m^{-2} via SKYRAD. 22DEC2015 can be contrasted with Regime 4's 31JAN2016, marked by larger negative mean doppler velocities, signifying updrafts within the cloud column. The radar reflectivity is indicative of ice in a mixed-phase cloud, due to the larger sizes of ice crystals when compared to liquid water droplets. Displaying large geometric thickness that erratically fluctuates over time, 31JAN2016 is an example of an orographically-induced cloud-system formed at the TAM upstream of Ross Island. Low attenuation of the lidar backscatter signal beneath the liquid layer (marked by high backscatter band) in conjunction with high depolarization below the liquid layer is a prime marker for ice crystal precipitation falling from a mixed-phase cloud.

3.6 Cloud Cover & Broadband Atmospheric Transmission

The variable *total_percent_cloud_cover* was created by summing the *percent_opaque* and *percent _thin* variables for each daily TSI file. Total cloud cover was then sorted into hourly averages using the TSI *time* variable as an averaging index. Many daily TSI files came split into two, or sometimes four data files. These partial files were then appended together, again using using the *time* variable as an index for sequential alignment of values within each array. Temporal gaps in the daily timeline of some TSI data files were replaced by “Not-a-Number (NaN)” placeholder values to act as array buffers so that each daily TSI data array had the same standard dimensions. Ignored during computation, NaN values acting as “array buffers” provide the means

to easily compare two datasets of unequal size, as long as proper time-indexing is maintained. Missing values in the TSI data are designated numerically by the value "-100", and were replaced with NaN values. The *total_percent_cloud_cover* arrays were then grouped using the k-means clustering regime, and appended by order of occurrence. A normalized histogram set to a 0–100% scale (percentage of occurrence within distribution) was used to visually display varying cloud fraction for each regime distribution. Histogram bid-width sizes were set to 10% (Figure 22).

The variable *down_short_hemisp* within the SKYRAD dataset represents broadband downwelling shortwave radiation (0.3 – 3.0 μm) in units of irradiance (W m^{-2}). Once each daily SKYRAD file is loaded, the *down_short_hemisp* variable was extracted for each day and assigned a variable name. To account for the influence of changing solar zenith angle throughout the day when calculating broadband atmospheric transmission, each *down_short_hemisp* variable was split into 24 segments of hourly data. SKYRAD samples once per minute, with each segment containing a set of 60 samples resulting in a 1x24 array of atmospheric transmission values per day. Hourly swaths occurring when the solar zenith angle < 85° were omitted from the calculations. Each hourly short irradiance segement was then loaded into its own transmission equation with unique zenith angle as a function of time. The purpose of these calculations is to compare the measured downwelling shortwave irradiance (via SKYRAD) to the solar constant (1361 W m^{-2}), which is corrected using a Earth-Sun distance correction (ESDC) value and modulated throughout the day by a time-variant "cosine(zenith angle)" factor, representing the angle of insolation incidence at the TOA. The values of hourly zenith angles at M1 were acquired using *NOAA's Solar Geometry Calculator*, and the daily ESDC was obtained using *Instesre's Solar Position Calculator*. The transmission equation is as follows:

$$T_{0.3-3.0\,\mu m} = \frac{F_{SKYRAD}}{F_{TOA}\cos_{deg}(SZA)\,f_{ESDC}}$$

where F_{SKYRAD} is represented by SKYRAD variable *down_short_hemisp*, and F_{TOA} = 1361 W m^{-2}. This equation compares the amount of downwelling shortwave irradiance measured at the surface to the solar constant as modulated by the solar zenith angle and ESDC. The resulting value is a dimensionless ratio (between 0 and 1) of the overall transmittance of incoming solar radiation reaching the surface compared to the hypothetical maximum for a given zenith angle and ESDC. This transmittance value provides insight into how much shortwave extinction occurs in the Earth's atmosphere. Once these calculations are complete for each day in DJF, the daily arrays are then processed by a grouping script as dictated by the *k*-means clustering algorithm. Once the daily atmospheric transmission arrays were appended together according to their regimes, histograms were created for each regime distribution based on percentage of occurrence (Figure 22). The histograms display how atmospheric transmission varies as a function of meteorological regime. Transmission values were then plotted as a function of *total_percent_cloud_cover* (via TSI) to gain insight into how varying cloud fraction affects atmospheric transmission, as well as determining particular sensitivities and thresholds within each regime as functions of cloud properties – inherently linked to the underlying meteorological regime origin.

In addition to downwelling hemispheric shortwave irradiance, the SKYRAD dataset includes the longwave compliment in variable *down_long_hemisp1*, which records measurements of incoming radiation (3.5 – 50 μm) in the infrared portion of the electromagnetic spectrum. Histograms of SKYRAD longwave were taken as a function of regime. SKYRAD longwave was then plotted as a function of cloud cover, in effort to see how varying cloud fraction affects

downwelling longwave.

Clouds absorb and emit in the longwave portion of the electromagnetic spectrum, thus making the *down_long_hemisp1* variable significant in that the longwave measurements are sensitive to specific cloud properties. In general, low-lying optically thick clouds tend to have warmer temperatures and are more reflective to shortwave irradiance; in contrast to higher, optically thin clouds, which have colder temperatures and thus more readily absorb longwave radiation. Over Ross Island, noticeable changes in downwelling longwave radiation can be observed as a function of varying cloud fraction. There are meaningful differences in the longwave emission characteristics from a liquid cloud originating from Ross Sea, juxtaposed with a mixed-phase cloud formed via orographic lifting over the TAM.

Downwelling longwave irradiance can be compared to shortwave atmospheric transmission values of the same regimes as a systematic "quality check". Generally, there is a coherent relationship between the two measurements; i.e. when atmospheric transmission drops, downwelling longwave increases. This can be generally interpreted as a proxy to cloud-presence, since shortwave extinction and longwave emission are likely to increase as the atmosphere transitions from clear-sky to increasing cloud cover.

The ARSCL variable *cloud_layer_base_height* provides a matrix of cloud base height and layer values as a function of elevation and time. Daily swaths of ARSCL cloud base height information were split in 24 hourly arrays, in which the median height value of the of lowest *cloud_layer_base_height* layer was used as input in the cloud base temperature algorithm.

The INTERPSONDE VAP provided a daily grid map of atmospheric temperatures as a function of height and time. This dataset was useful in correlating temperature with cloud base, since cloud movement can be highly variable on both spatial and temporal scales throughout each

day. An algorithm was developed to take each ARSCL cloud base median value and match it with the corresponding INTERPSONDE temperature value for the same height and time denoted by the ARSCL cloud base median input. Prior to the execution of this algorithm, the INTERPSONDE gridded matrix was hourly averaged, to be consistent with the ARSCL cloud base array. This ensured both variables were time-aligned. The height index within INTERPSONDE dataset was also converted from km to m, to be consistent with that of the ARSCL height index. For each cloud base height median value, the algorithm compares the cloud base value with the INTERPSONDE height value (recorded in increments of 20 meters). If the INTERPSONDE height value is less than the cloud base height, the algorithm continues to iterate until an INTERPSONDE height value is either greater than or equal to the cloud base height value. The algorithm then takes this INTERPSONDE height value and co-locates the corresponding INTERPSONDE temperature value for the given height and time. This effectively matches the cloud base height with the appropriate temperature based on height and time of day, with a vertical accuracy of less than 20 meters (Figure 24).

ARSCL cloud variables were also used to manually derive cloud geometrical thickness by subtracting the lowest layer value of "*cloud_layer_base_height*" from the highest layer value in "*cloud_layer_top_height*" as a function of time. Once the resulting data is sorted into regimes, histograms are computed for each regime distribution, to gain perspective on cloud thickness and how it can be related to meteorological regimes of varying origin (Figure 23). For instance, Regime 4 has the largest average cloud thickness, which may be linked to its origin of formation; moisture originating from the Southern Ocean, advecting south by southwest over WAIS and RIS, then being orographically lifted by the TAM, resulting in thick mixed-phase clouds due to mountainous forcing causing moisture to be rapidly lifted and cooled. The expected phase change

due to below-freezing temperatures does not necessarily occur, simply due to the lack of ice condensation nuclei. This in turn in results in clouds being partially composed of "supercooled" liquid with temperatures far below the freezing point of water (as low as -40°C).

Particular cases of interest are then corroborated by EOSDIS NASA imagery, such as the mixed-phase, orographic-lifting case of 31JAN2016 (Regime 4; Figure 1a); which can be contrasted with the predominantly liquid-phase, marine air advection case of 22DEC2015 (Figure 1b). Notice the difference in cloud properties – indicative of origin and travel path – as a function of mesoscale/synoptic meteorological regimes, which can then be correlated to particular modes of the SAM, as HP ridges and LP troughs vary meridionally and zonally over time.

3.7 Influence of Phase on Cloud Optical Depth

We used MFRSR and MFR datasets to acquire precision measurements at 870 nm, a part of the shortwave spectrum where absorption by atmospheric trace gases is negligible and cloud particle scattering is independent of wavelength. The MFRSR instrument faces skyward to measure downwelling solar irradiance, whereas the MFR instrument faces downward to measure upwelling reflected solar irradiance. These spectral radiometers use silicon photodiode detectors (in contrast to the thermopiles used in SKYRAD/GNDRAD) to acquire precise measurements of specified narrowband channels in the shortwave spectrum. The 870 nm channel samples the most transparent atmosphere in the shortwave, and in turn, used as the reference wavelength in MFRSR aerosol optical depth retrievals. The MFRSR variable *hemisp_narrowband_filter5* gives total downwelling hemispheric irradiance for the 870 nm channel.

Cloud extinction at 870 nm, and hence the cloud optical depth, is independent of wavelength for nearly all cloud liquid water droplets or ice particles in the real Earth atmosphere. This is because at this shorter wavelength the cloud particles only scatter (redirect) radiation but do not absorb radiation. However at wavelengths longer than ~1100 nm (into the near-IR), cloud particles begin to absorb as well as scatter radiation. This absorption is ultimately related to the spectral dependence in the complex refractive index of the scattering medium, and this spectral dependence is different between liquid water and ice. Generally speaking, nearly all realistic cloud ice crystals absorb more near-IR radiation than their comparably sized liquid water counterparts.

As wavelength increases to approximately 1.6 μm, the difference between liquid water and ice particle extinction (scattering plus absorption) becomes more pronounced. Since the broadband measurements via SKYRAD cover 0.3 – 3.0 μm, they can be expected to show variability related to the relative presence or absence of ice in a cloud. However, narrowband irradiance at 870 nm responds only to wavelength-independent extinction (scattering only), and any combination of phase, particle size, and water content that together yield a given value of the optical depth will show the same transmission of the 870 nm irradiance to the surface. This is observed when plotting narrowband transmission against broadband transmission in Figure 9. The narrowband and broadband samples used in this plot were constrained using a TSI total percent cloud cover threshold of 95%, signifying optically thick overcast clouds. Upon comparison to other regimes, Regime 4 exhibits a slightly lower broadband transmission at the same narrowband transmission value within the narrowband transmission range of ~0.4 – 0.7 (Figure 10). As narrowband transmission increases in the 0.4 – 0.7 range, Regime 4 exhibits greater downwelling broadband attenuation, resulting in lower broadband atmospheric

transmission. We hypothesize that this can be attributed to characteristics of mixed-phase clouds, i.e., ice attenuates more than liquid water in the near-infrared range. This clue shown by the slight difference in measured flux at the same cloud optical depth – may be is useful in distinguishing differences in phase properties between cloud-systems. Narrowband transmission (T_{870nm}) is calculated using the following equation:

$$T_{870\,nm} = \frac{F_{MFRSR\ Filter\ 5}}{F_{TOA\,(870\,nm)} \cos_{deg}(SZA)\, f_{ESDC}}$$

where derived solar constant, $F_{TOA\,(870\,nm)}$ = 0.9376 W m^{-2}; used in combination with hourly averaged solar zenith angles (SZA) and appropriate Earth-Sun distance factors (ESDC), calculated as a function of time. Calculated values of narrowband transmission were then temporally matched with broadband transmission values, and constrained by a TSI calculated cloud fraction of ≥ 95% total cloud cover, signifying overcast skies. Once this cloud fraction criteria was met, time-matched characteristics of other critical variables were obtained to calculate τ_c, which include: α_{870nm} (narrowband albedo) and $\alpha_{0.3\,-\,3.0\,\mu m}$ (broadband albedo). The daily-averaged narrowband albedo was computed by dividing the daily upwelling 870 nm narrowband irradiance (MFR) by the daily downwelling 870 nm narrowband irradiance (MFRSR) in Figure 8. An analogous process was used to calculate the broadband albedo, by dividing the GNDRAD upwelling irradiance by the SKYRAD downwelling irradiance.

Cloud optical depth (τ_c) is a dimensionless quantity representing the radiative extinction efficiency of a cloud layer along the incidental path length. Values of τ_c were derived using the narrowband transmittance and albedo values using the radiative transfer model of Lubin and Vogelman (2011). For a given SZA and surface albedo, the model is run iteratively at 870 nm,

gradually increasing the trial cloud optical depth until the calculation matches the MFRSR measurement. A similar approach is used by Fitzpatrick et al. (2004) and by Fitzpatrick and Warren (2005; 2007). The extinction efficiency of a cloud is a factor of the density of cloud particles along the path of incidence, integrated over the total cloud thickness:

$$\tau_{c(870\,nm)} = \int_{CB}^{z} k_{scatter}\,\rho_{cloud\ particles}\,dz$$

$$\tau_{c(870\,nm)} = \left(\frac{3}{2}\right)\left(\frac{LWP}{r_e}\right)$$

where LWP is Liquid Water Path (g m^{-2}) and r_e is the effective droplet radius, which is the ratio of the third to the second moment of the cloud droplet size distribution. The narrowband (870 nm) optical depth values are then used to sort the time-associated broadband irradiance values into equal-sized bins as a function of incremental zenith angle ranges. Once the values are sorted, differences are calculated between regimes in attempt to isolate subtle changes in irradiance as a result of varying cloud phase. This allows for the comparison of regime's downwelling broadband signature when held at the same τ_c and SZA (because downwelling shortwave radiation depends strongly on both). In the hypothetical scenario of two adjacent clouds with equal optical thickness and SZA – one cloud composed entirely of liquid water and the other cloud of the mixed-phase variety – a broadband radiometer at the surface would measure more downwelling shortwave irradiance when placed below the liquid-water cloud. This is due to the supplemental ice absorption of the mixed-phase clouds, attenuating slightly more in the near-infrared.

Subtle differences in irradiance between the meteorological regimes and associated cloud-systems become evident upon the sorting of broadband measurements via optical depth retrievals and varying solar zenith angle. Discerning the differences in radiative extinction trends between the regimes gives us clues toward understanding cloud composition, and how this varies with meteorology. In this case, determining differences in the possible effects of cloud phase by way of a conservative-scattering cloud optical depth index is shown to be a useful indicator in identifying differences between regimes.

Using a 2-hour stationary time-series from 11DEC2015 (1500-1700Z) where the downwelling flux and τ_c exhibited stationary trends, we examined the effects of autocorrelation for every minute, from lag-1 to lag-20. For downwelling flux, lag-1 and lag-2 showed large autocorrelation, at > 0.95 and > 0.85 respectively. By lag 10, the autocorrelation had reduced to approximately 0.03. For τ_c, lag-1 and lag-2 showed similar large autocorrelation values, at 0.96 and 0.9 respectively. The τ_c lag-10 came out to be 0.54. To mitigate these effects of autocorrelation – which results from the high-resolution sample rate – the sample rate was changed from 1 to 10 minute averages. We then checked the same time period on 11DEC2015 with the new 10 minute average sample rate. The flux lag-1 reduced to ~0.12, and τ_c lag-1 reduced to ~0.55. We then applied the following formula to estimate the effective sample size:

$$N_{eff} = N\left(\frac{(1 - r1 * r2)}{(1 + r1 * r2)}\right)$$

where N_{eff} is the effective sample size, N is the nominal sample size, r1 is the lag-1 autocorrelation of flux, and r2 is the lag-1 autocorrelation of τ_c. This decreased the sample size by a factor of 0.88 (Bretherton et al., 1999).

Section 4

Results

4.1 Regime Comparisons

Using the results from the regime τ_c calculations, downwelling shortwave flux was plotted as a function of "Cloud Optical Depth Bin", to demonstrate the effect of increasing τ_c on downwelling shortwave. The values depicted on each plotted curve were constrained by a limited SZA range of 5°, with the entire SZA range bounded from 55° to 80°. This resulted in five plots for each of the three major regime pairings (Regime 3 was excluded due to small sample size coming from only one small part of the summer 2015-2016 season). In some cases of regime comparison, discerning differences between the the plotted curves proved difficult; to better visualize any incongruous behavior between attenuation curves, another set of plots were created to display the difference in flux between the two regimes being compared. Student's *t*-test statistics are also included on these plots, with a t-statistic > ~2 generally representing significance; in other words, it is highly probable that the two sample distributions being compared come from different parent distributions. Next, a table of comparisons (Figure 19) summarizes the shortwave findings between regimes, including data such as bins per regime-pairing, percentage of bin difference > 0, and associated statistical significance of bins and bin differences. The last set of regime-pairing plots concerned the effect of τ_c on downwelling longwave (Figures 20 and 21). In this case, only one plot is necessary for each regime-pairing, due

to SZA being a non-factor concerning downwelling longwave. Similarly to the shortwave above, a corresponding set of longwave-differences with associated t-statistics are plotted. All longwave τ_c values greater than 10 were grouped as one single bin, representating a blackbody-like cloud.

4.2 Regime 1 & 2

Regime 1 and Regime 2 (Figures 13 and 14) display parity in terms of τ_c and cloud properties at all measured SZA. There is slight difference in SZA range 55°-60° (represented by plot A in Figure 13), with Regime 1 attenuating more shortwave with increasing τ_c, showing strong statistical significance with a shortwave flux difference of greater than 20 W m^{-2}. This can be ascribed to the thicker liquid-dominated clouds via marine-air advection of Regime 1. However this regime-flux relationship reverses as Regime 2 attenuates more shortwave as SZA increases slightly, and continues to alternate as SZA approaches the measured maximum; again showing no strong distinction between Regime 1 and Regime 2 in terms of downwelling shortwave. This is reflected in the shortwave summary table, with only 52% of optical depth bins showing N difference greater than 0., exhibiting a weighting average difference of -2.6 W m^{-2}.

A stronger distinction between Regimes 1 and 2 occurs in the longwave, due to cloud temperature. Matching cloudbase height provided by ARSCL with the gridded temperature VAP product provided by INTERPSONDE, Regime 1 was found to have the warmest average cloudbase temperature of -15.55°C (Figure 24). Results are also corroborated upon measurement of average downwelling longwave via SKYRAD, with Regime 1 showing the largest average downwelling longwave flux of 234.8 W m^{-2}(Figure 22). Regime 2 favors large-scale subsidence and subsequent continental air outflow, and is denoted by the lowest average TSI cloud fraction (40.96%; Figure 22), lowest average cloudbase temperature (-18.3°C), and lowest average downwelling longwave

flux (217.1 W m^{-2}) of all regimes. Regime 1 consistently emits an average of 10 W m^{-2} more than Regime 2 at $\tau_c \leq 10$, with strong statistical significance. However, this relationship reverses at $10 \leq \tau_c \leq 15$, with Regime 2 emitting approximately 10 W m^{-2} more than Regime 1 until $\tau_c = 20$. This trend continues across all regime-comparisons at ~277 W m^{-2}. There is an overall weighted LW difference of 5.6 W m^{-2}, and 7.7 W m^{-2} when τ_c is restricted to bins 1-10. This large difference in flux can be attributed to cloudbase temperature.

4.3 Regime 1 & 4

Regime 1 and Regime 4 (Figures 15 and 16) show a stark contrast in terms of shortwave attenuation at fixed optical depth and SZA range. This is evident in the flux-difference plots, displaying a majority of positive flux differences – signifying that Regime 4 is consistently attenuating more downwelling shortwave than Regime 1. This can be associated with the meteorological pattern ascribed to Regime 4. Large-scale cyclonic flow persists over the Ross Sea, setting up intrusion of marine-air over WA with southerly outflow over RIS. The TAM plays a significant role in the circulation patterns of Regime 4, with the orographic forcing causing rapid cooling to the advecting marine-air, resulting in the formation of thick, mixed-phased clouds upstream of Ross Island. These southerly advecting airmasses are then subject to complex atmospheric dynamics including katabatic winds, low-level jets, and barrier winds. Using ARSCL measurements to calculate cloud geometric thickness from cloudbase and cloudtop height detection layers, Regime 4 showed the largest average cloud thickness (3292m) of all regimes by more than 800m (Figure 23), as well as having the most diversity of geometrical thickness depths. Regime 4 also exhibited the lowest average broadband transmission (0.52; Figure 22) and largest average TSI cloud cover percentage (54.6%). The Regime 1 and 4 pairing exhibits the

largest total of statistically significant bins at 6, while exhibiting an average weighted difference of 6.6 W m^{-2}.

Regime 1 and 4 also differ in terms of downwelling longwave in a similar fashion to that of the Regime 1 and Regime 2 longwave relationship. Regime 4 emits less longwave than Regime 1 at smaller cloud optical depths, but at τ_c = 15, the relationship reverses. While Regime 1 has largest average downwelling longwave of all regimes, its maximum downwelling longwave value of 291.27 W m^{-2} is exceeded by the maximum value of Regime 4, 309.32 W m^{-2}. This can be attributed to large geometric cloud thickness of Regime 4, along with with its erratic structure due to the unique terrain-induced cloud-dynamics. There is an overall weighted LW difference of 3.6 W m^{-2}, and 5.2 W m^{-2} when τ_c is restricted to bins 1-10.

4.4 Regime 2 & 4

Similar to the shortwave comparison between Regime 1 and 2, Regimes 2 and 4 differ strongly in SZA range 55°-60° (Figures 17 and 18) , with Regime 4 attenuating more shortwave with increasing τ_c. Differences in shortwave flux magnitude for the remaining SZA ranges show 14 of 25 bins with positive differences, with an average weighted difference of 10 W m^{-2}. There is also parity in terms of downwelling longwave flux, showing small differences with a lower average statistical significance. There is an overall weighted LW difference of -1.4 W m^{-2}, and -1.9 W m^{-2} when τ_c is restricted to bins 1-10.

Section 5

Discussion

5.1 Supplemental Ice Water Absorption

A large portion of the meteorology observed over Ross Island originates from intense cyclonic activity over the Southern Ocean. A study conducted by Scott and Lubin (2016) compared Ross Island to Arctic-based sites Barrow, Alaska, and Summit, Greenland, and was found to have the largest IWC contribution to cloud optical depth at colder temperatures, demonstrating the strongest influence on the shortwave flux. The IWC in summer clouds was found to account for 17.5 W m^{-2} reduction of the total shortwave flux. The same IWC was found to have a lesser effect on the longwave flux, due to Ross Island having intermediate cloudbase temperatures compared to the two Arctic sites. This is due to the already significant effect of LWC on cloud optical depth, resulting from a larger density of longwave absorbers due to cloud droplets at Ross Island possessing the smallest effective radii (Scott and Lubin, 2016). The polar environment of WA gives rise to unique circulation patterns that manifest frequently in unique mixed-phase cloud-formational processes via orographic forcing, and can be observed downstream at Ross Island by way of mean-southerly flow of katabatic and barrier wind confluence zones (Scott and Lubin, 2016).

IWC within clouds plays a significantly different role than LWC at specific spectral ranges throughout the electromagnetic spectrum. Below 1100 nm, ice and liquid water scatter

conservatively, meaning no light is lost in the process of scattering. Above 1300 nm, the phase difference in absorption becomes readily apparent, as ice attenuates more solar irradiance than liquid water at the same optical depth. This is particularly evident in the 1600 nm and 2200 nm spectral windows (Scott and Lubin, 2014).

Albedo in the 870 nm range does not play a significant role in influencing the measured downwelling shortwave flux, due to a large amount of exposed basaltic rock during the summer season at Ross Island, as opposed to reflective snow cover in other seasons. The shape of ice crystals widely varies through differing shapes, sizes, and habits. Subsequently, these qualities each play a role in an ice crystal's unique radiative properties. Larger ice particles attenuate more than smaller ice particles at the same scattering optical depth (Scott and Lubin, 2014).

5.2 Synoptic Meteorological Drivers & the SAM Connection

The Antarctic Oscillation (AAO) – also known as the Southern Annular Mode (SAM) – defines the westerly movement of atmospheric geopotential fields in the high latitudes of the Southern Hemisphere. As the mean synoptic flow travels from west to east, transverse oscillations occur as a result of atmospheric dynamical forcings. The polar regions possess a stronger inertial effect on overlying air masses as a result of the apparent Coriolis force, which is then balanced by the PGF in order to achieve geostrophic balance (Lefebvre 2004).

Various meteorological data show recurring statistical patterns that emerge as result of atmospheric fluid force-balancing between the left-deflecting Coriolis force and PGF. These wave motions are analyzed and classified as phases of the SAM. Upon comparison to the background

average, the two modes of SAM that deviate most from the mean are categorized as “positive SAM phase” and “negative SAM phase”. The positive SAM phase is associated with anomalously low pressure fields over Antarctica, resulting in an intensified pressure slope extending from the mid-latitudes. This allows for stronger zonal flow over the Southern Ocean. The negative SAM phase is associated with anomalously high pressure fields over Antarctica, resulting in weaker zonal flow over the Southern Ocean due to a more shallow pressure slope extending downwards from the mid-latitudes. Using results from this study, associations can be made by correlating Regime 1 and Regime 3 with negative SAM phase, and Regime 2 and Regime 4 with positive SAM phase.

Section 6

Conclusion

The role of clouds on the physical state of West Antarctica's frozen-freshwater reservoir is highly significant, as clouds serve as atmospheric conduits – linking energy and moisture transport from low to higher latitudes, resulting in a strong influence on downwelling radiation and precipitation fields above large ice masses. This CRE provides a significant amount of radiative energy involved in the surface melt (Scott and Lubin, 2017). The effects of clouds are shown to modulate the duration and intensity of cryospheric large-scale melt events (van Tricht et al., 2016).

Clouds possess great influence on the SRB in the Antarctic (Scott and Lubin, 2016). A net warming effect via cloud forcing was shown in Nicolas et al. (2017), using AWARE data to demonstrate the enhancement of RIS/WAIS surface melt due to CRE. A better understanding of the link between the cloud radiative forcing on SRB, and its link to large-scale meteorology, is essential knowledge that needs to be acquired through this type of polar data analysis.

The goal of this study was to explore the relationships between underlying meteorology (influenced by terrain) that give rise to cloud microphysical variability and in turn, modulate downwelling radiation over a site such as Ross Island. Continued analysis of AWARE data will lend to a greater understanding of the effect of warming global temperatures on West Antarctica (which is inexorably linked to global sea level rise), to which data from Ross Island can serve as a

benchmark for scientific comparison. With current climate-warming phenomena such as the calving of Larsen-C Ice Shelf and gradual loss of Thwaites and Pine Island Glaciers, improving our understanding of the Antarctic atmosphere and its influence on the great ice sheets becomes increasingly important.

This thesis in part is currently being prepared for submission for publication in a peer-reviewed journal, with coauthors Scarci, Kris; Scott, Ryan; and Lubin, Dan. The thesis author was the primary investigator and author of this material.

Figure Appendix

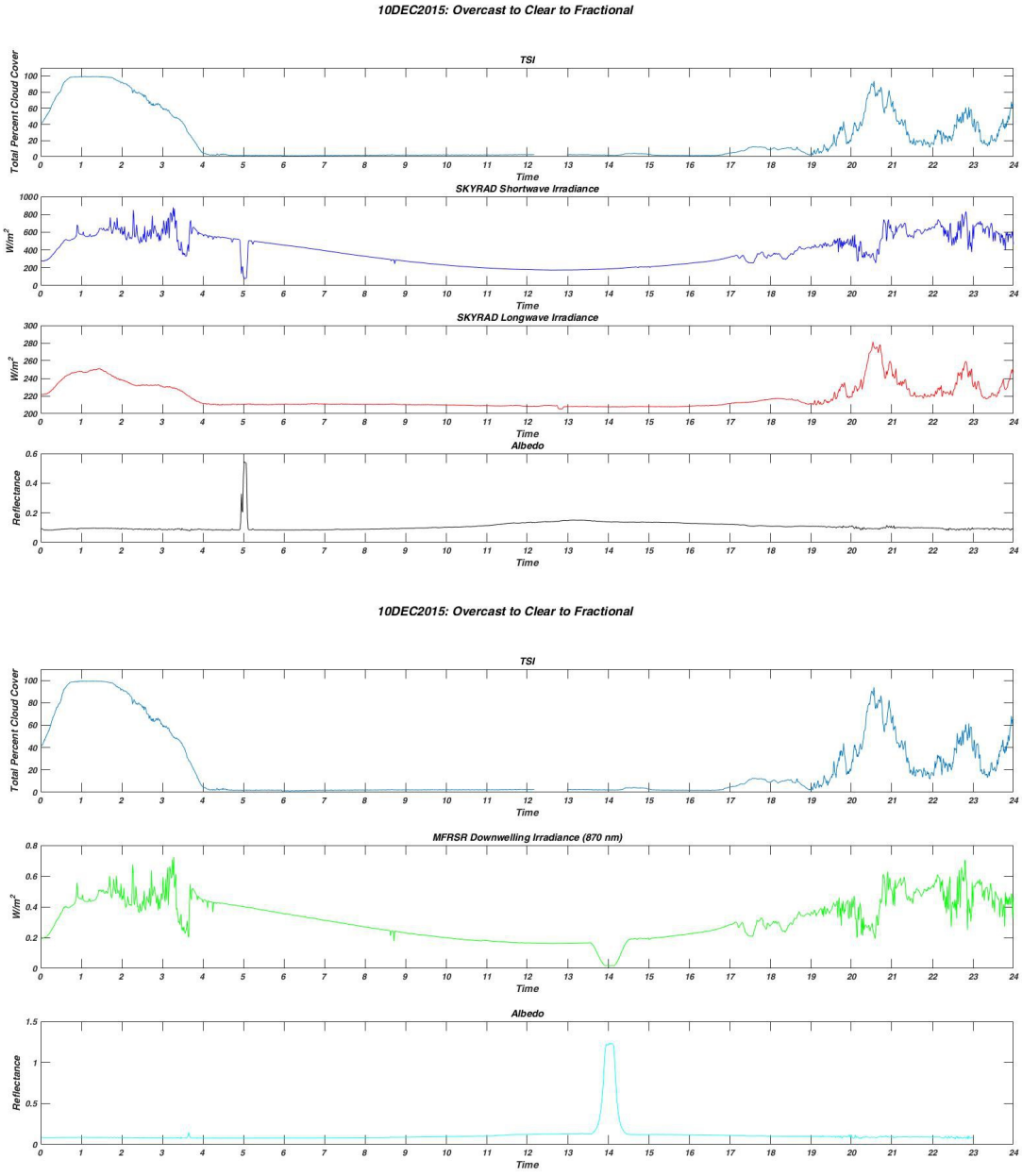

Figure 1a: 10DEC2015 Example Case – Overcast to Clear-Sky to Fractional Cloud Cover. The top four time-series plots represent downwelling broadband flux and albedo, while the bottom three represent downwelling narrowband flux and albedo.

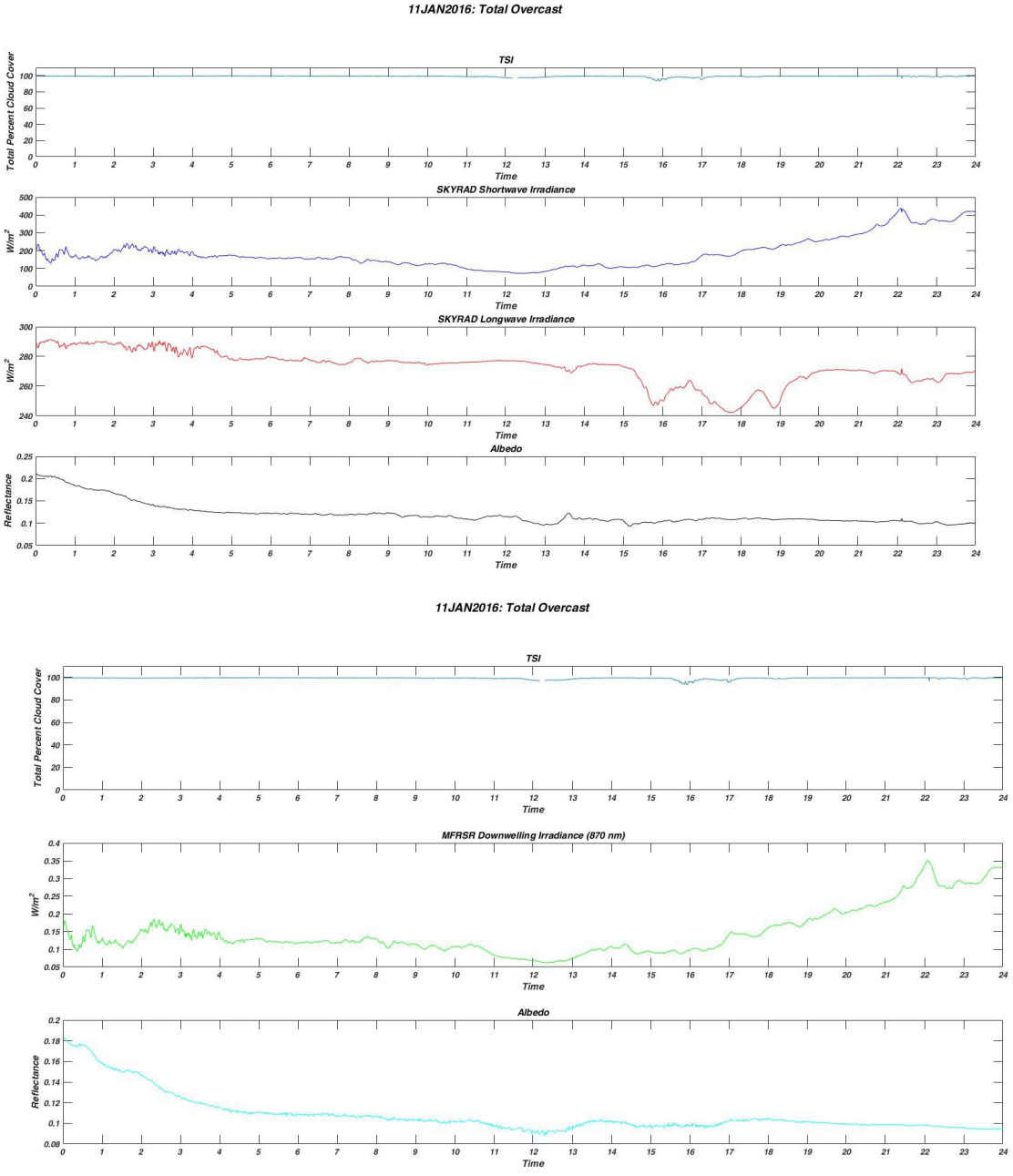

Figure 1b: 11JAN2016 Example Case – Total 24hr Overcast. The top four time-series plots represent downwelling broadband flux and albedo, while the bottom three represent downwelling narrowband flux and albedo.

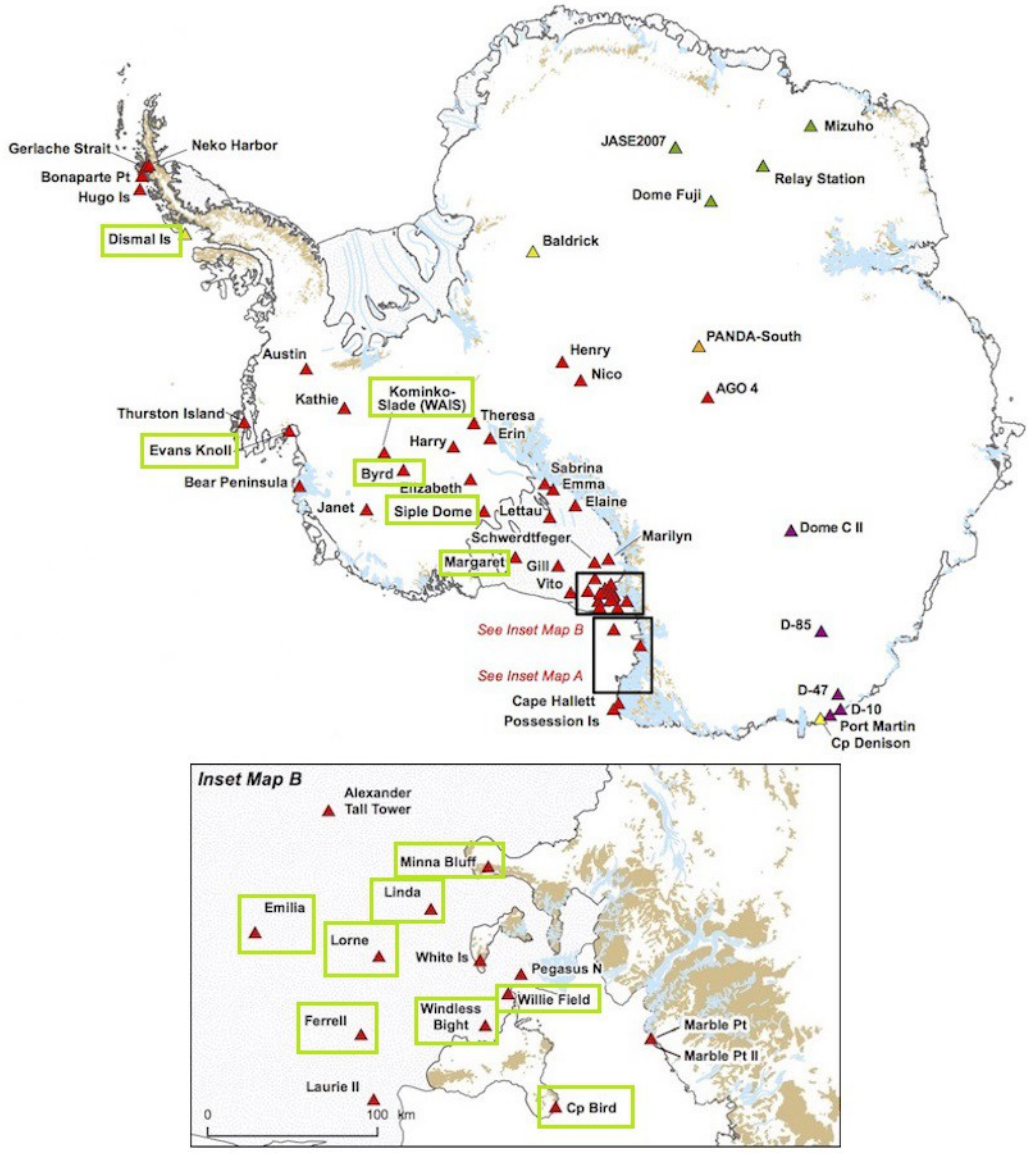

Figure 2: Map of AWS Stations in Antarctica – 2018 (Courtesy of Space Science & Engineering Center, UW-Madison). Locations of AWS Stations used in this study are enclosed in green rectangles. Inset Map B showcases stations in close vicinity to Ross Island, with Willie Field serving as the main airfield for McMurdo Station and New Zealand's Scott Base, Ross Island. Locations of interest across WA include Dismal Island (proximal to Larsen Ice Shelf), Evans Knoll (Pine Island, proximal to Thwaites Glacier), Siple Dome (proximal to WAIS melt event, 2016), and Kominko-Slade (WAIS Divide).

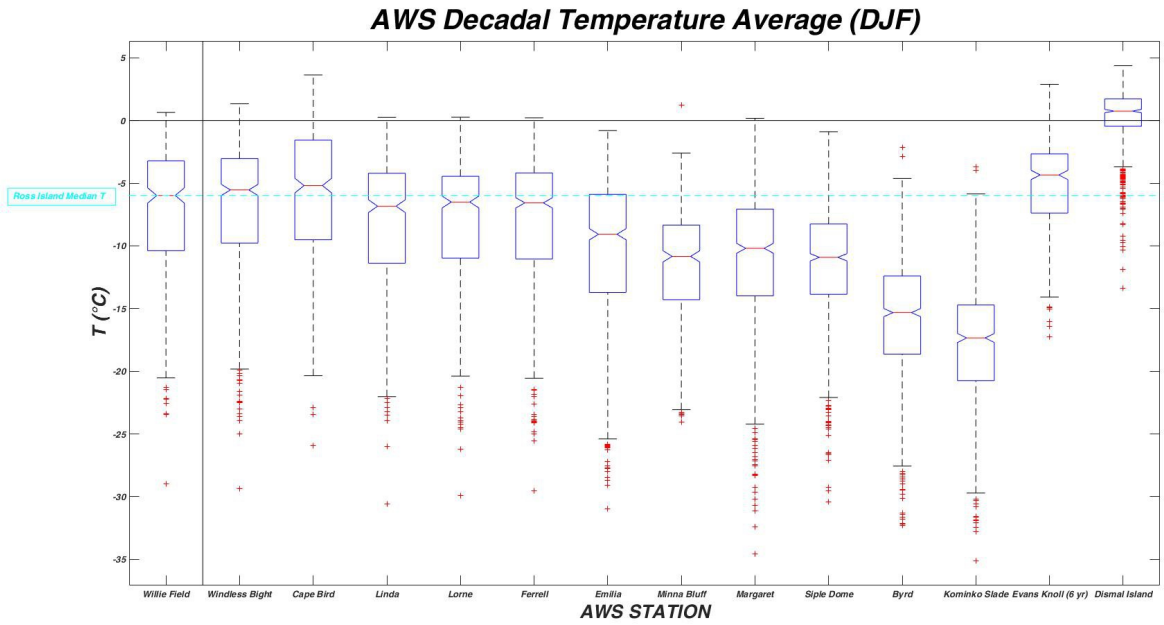

Figure 3: Boxplots representing the decadally averaged summer temperatures (2007 – 2016) for multiple AWS stations across WA. The leftmost boxplot (Willie Field) represents the most proximal location to McMurdo, Ross Island, with the dashed-cyan line depicting the its median decadal temperature (-5.98°C). Stations are ordered by spatial proximity to Willie Field (left to right). Median values are represented by horizontal red dashes within each boxplot. Bottom and top edges of each box represent 25th and 75th percentiles respectively. The whiskers extend to the most extreme data points not considered outliers, and the outliers are plotted as red "plus" signs.

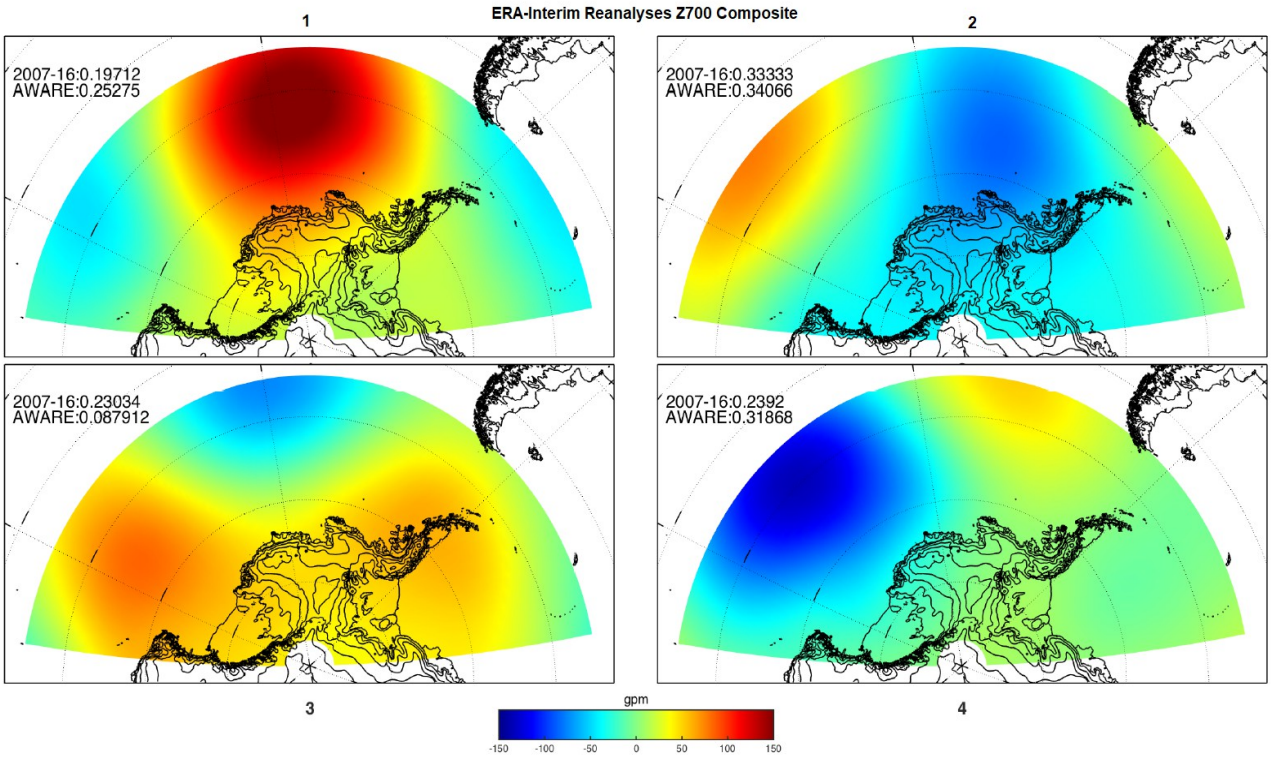

Figure 4 (courtesy of Ryan Scott): Composite results from the k-means clustering of decadally-averaged geopotential height fields (Z700) using ERA-Interim Reanalysis data for West Antarctica, depicting geopotential anomalies in gpm (geopotential meters). Warm colors represent high pressure riding, whereas cold colors represent low pressure troughing (Scott et al., 2018).

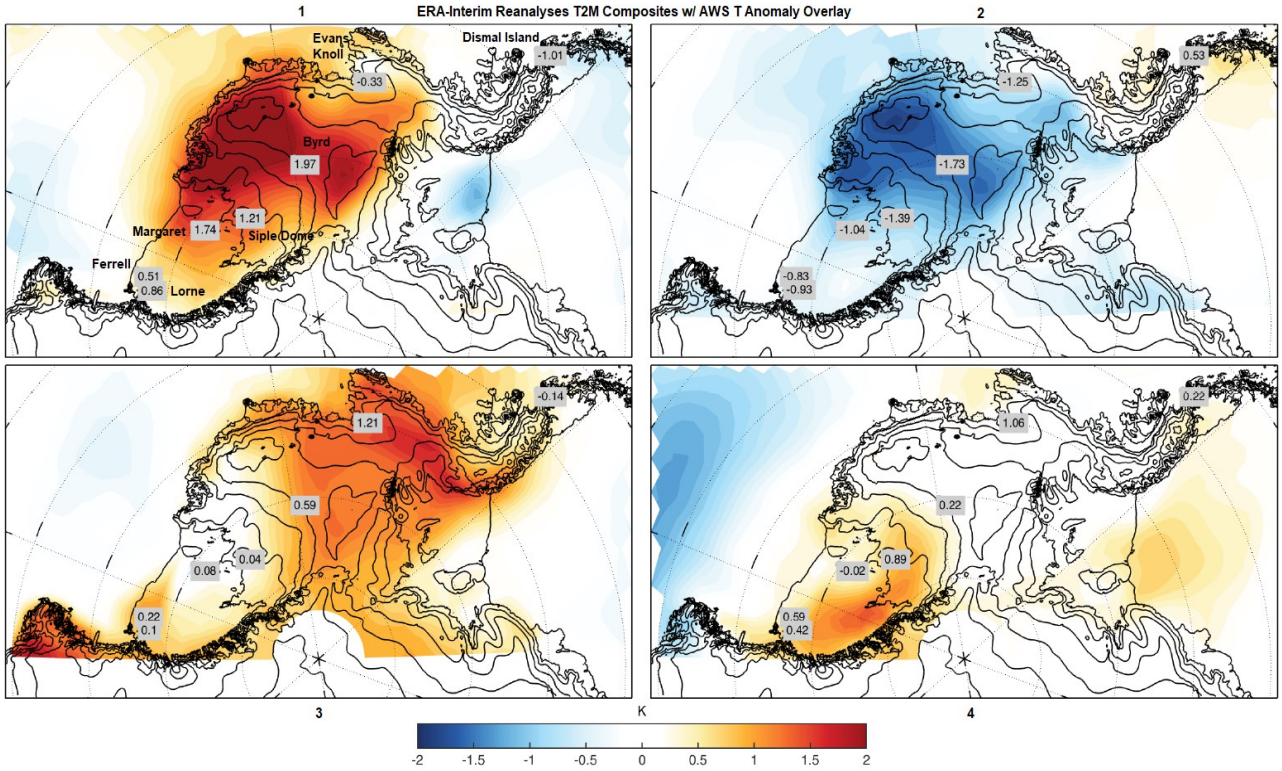

Figure 5 (courtesy of Ryan Scott): Composite results from the k-means clustering of decadally-averaged surface temperature (T2M) measurements using ERA-Interim Reanalysis data for West Antarctica. Shaded colors represent temperature anomalies in Kelvin. Superimposed on each regime plot is an overlay of decadally averaged surface temperature anomalies for selected AWS stations (Scott et al., 2018).

	DEC2015	JAN2016	FEB2016
Regime 1	9,10,11,12,13,20,21,22,23,24,25,26,27	6,7,8,9,10,11,12,13,14,15	none
Regime 2	1,2,3,8,18,19,28,29,30	20,21,22,23,24,25,26,27,28,29	8,11,12,13,14,15,16,17,18,19,20,21
Regime 3	14,15,16,17,31	1,2,3	none
Regime 4	4,5,6,7	4,5,16,17,18,19,30,31	1,2,3,4,5,6,7,9,10,22,23,24,25,26,27,28,29

Figure 6: Table of k-means sorted days by regime.

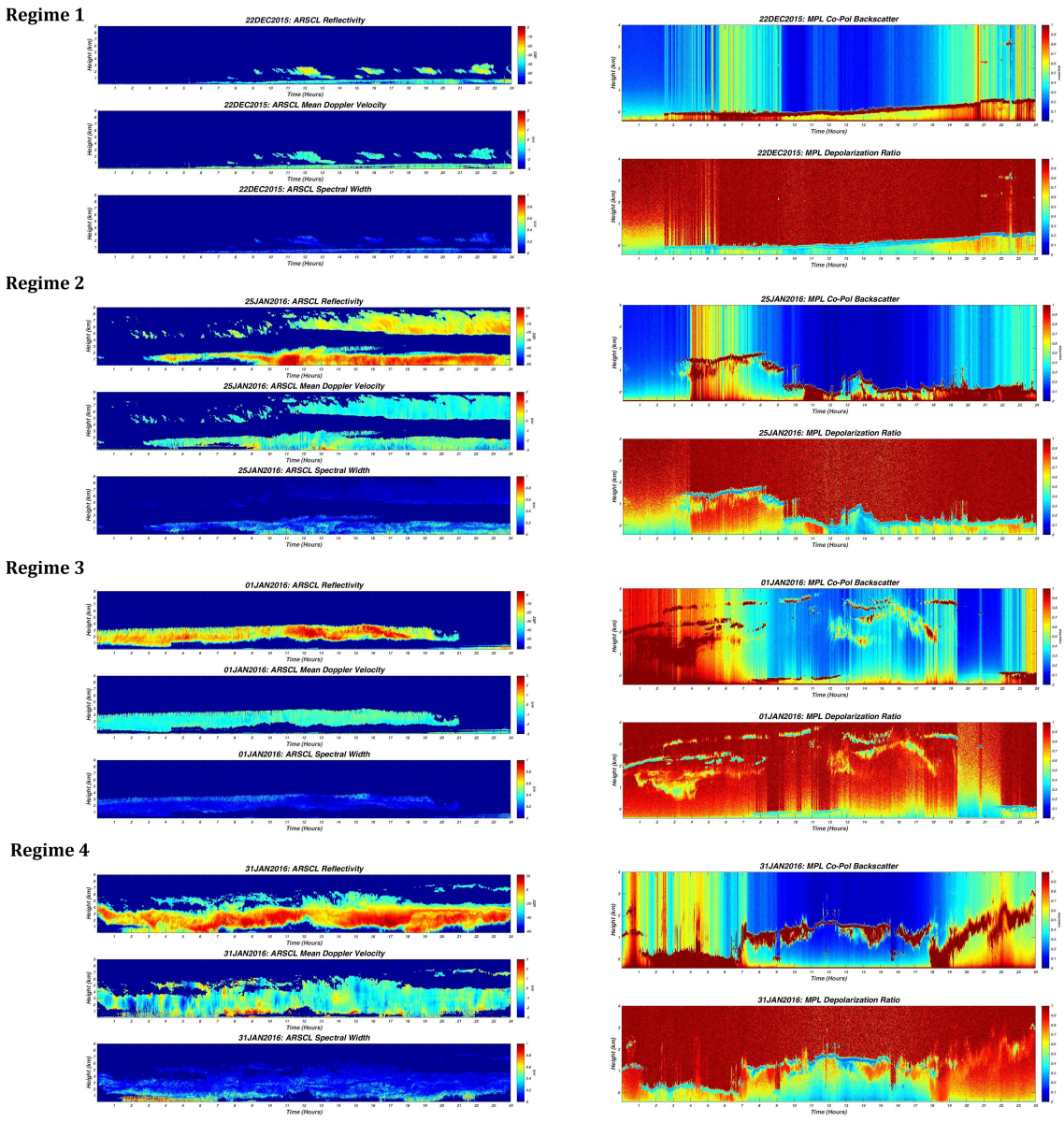

Figure 7: KAZR (via ARSCL) and MPL plots for representative days of each regime. KAZR (radar) plots are stacked in the left column, and consist of Reflectivity, Mean Doppler Velocity, and Spectral Width. MPL (lidar) plots are stacked in the right column, and consist of Co-Polarized Backscatter and Depolarization Ratio.

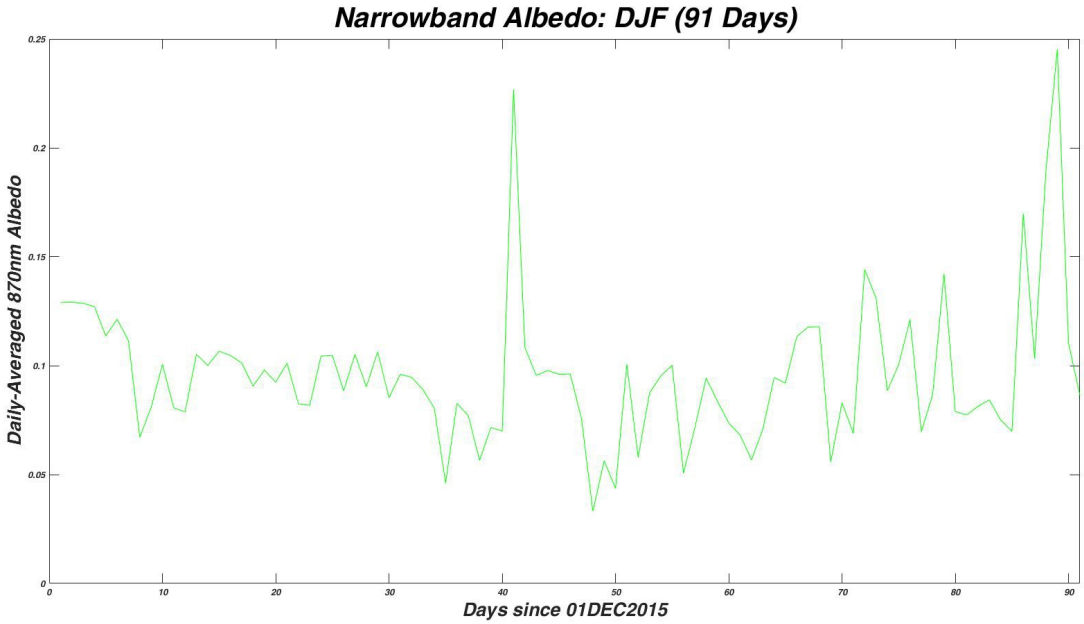

Figure 8: Time-series of daily-averaged 870 nm surface albedo during DJF at Ross Island.

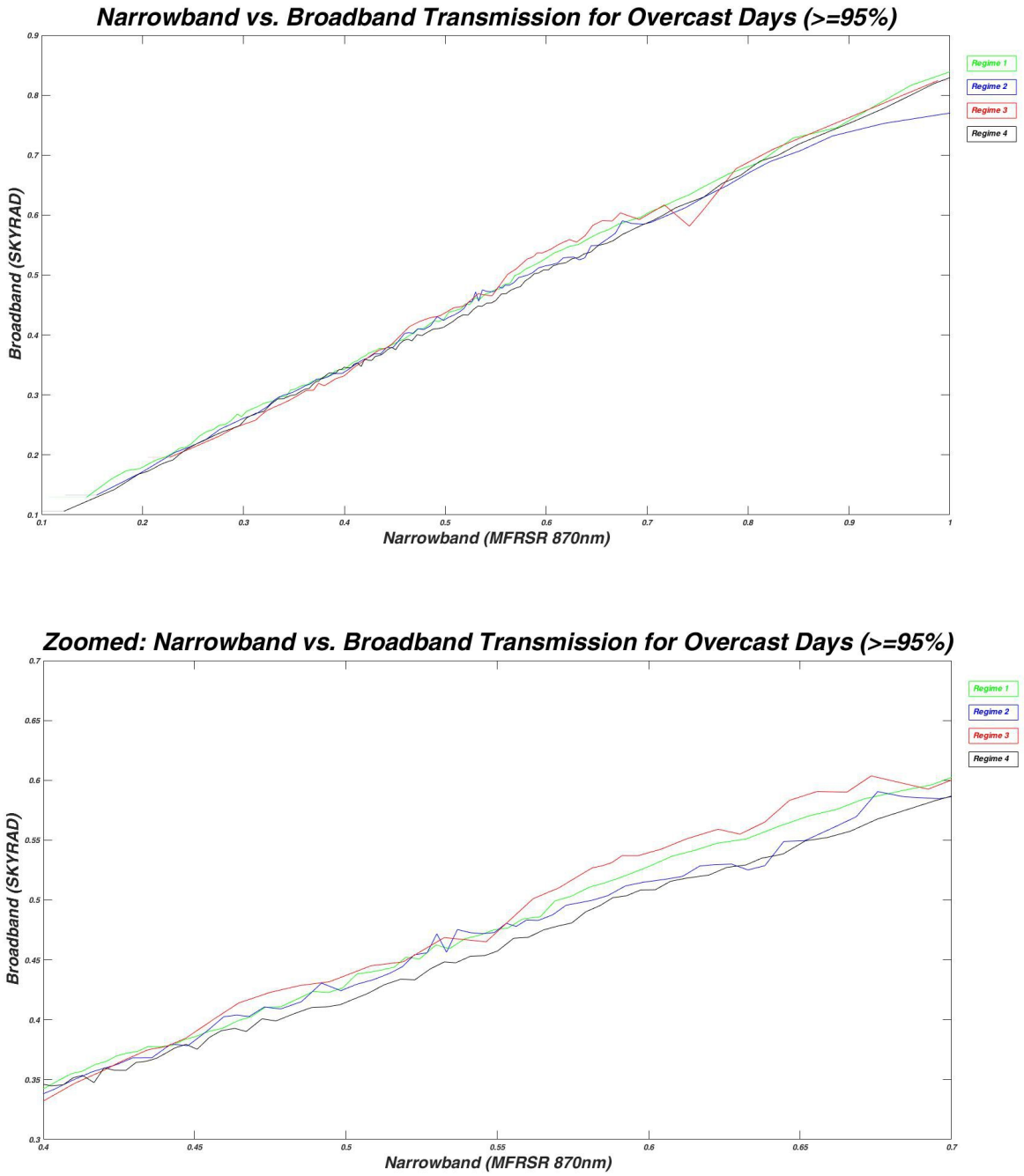

Figure 9-10: MFRSR Narrowband (870 nm) Atmospheric Transmission plotted as a function of SKYRAD (300 – 3000 nm) Broadband Atmospheric Transmission for each regime. Samples were constrained using a TSI total percent cloud cover threshold of ≥ 95%, signifying optically thick overcast clouds. Upon comparison to other regimes, Regime 4 exhibits a slightly lower broadband transmission at the same narrowband transmission value within the narrowband transmission range of ~0.4 – 0.7. As narrowband transmission increases in the 0.4 – 0.7 range, Regime 4 exhibits greater downwelling broadband attenuation, resulting in lower broadband atmospheric transmission. This can be attributed to characteristics unique to mixed-phase clouds; ice attenuates more than liquid water in the near-infrared range.

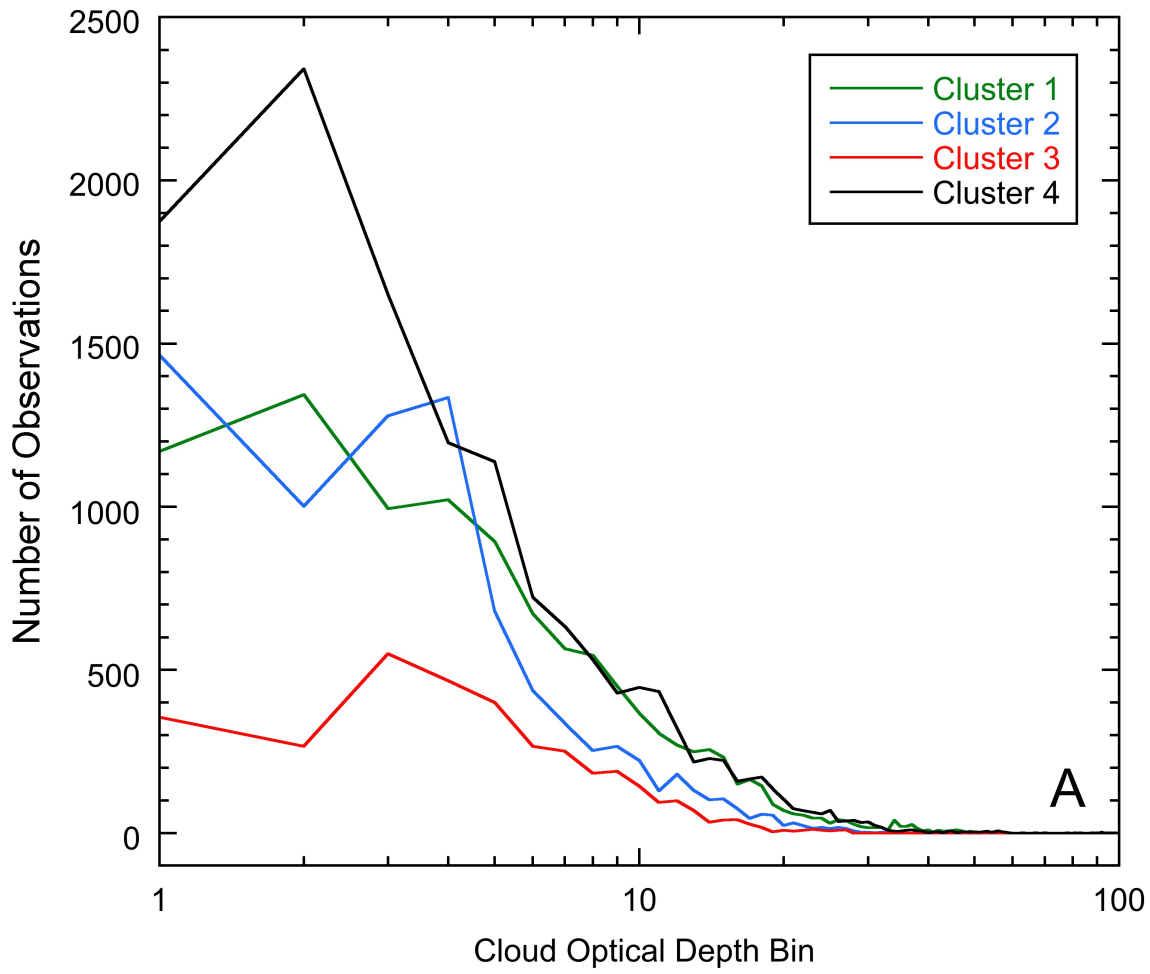

Figure 11: Line plot depicting number of retrieved cloud optical depth observations per regime-cluster distribution.

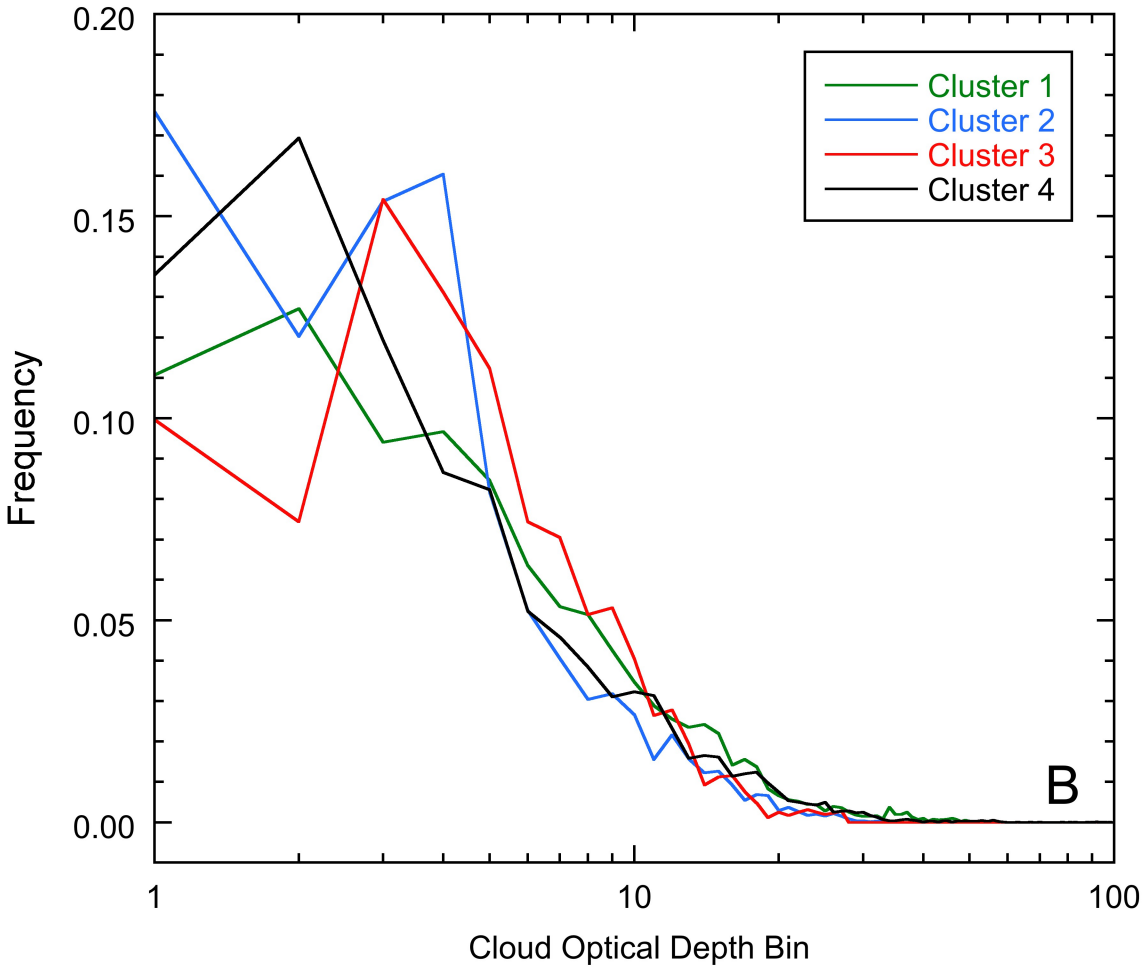

Figure 12: Line plot depicting frequency of occurrence of retrieved cloud optical depths per regime-cluster distribution. This plot is qualitatively similar to that of Figure 9 of Fitzpatrick et al. (2004).

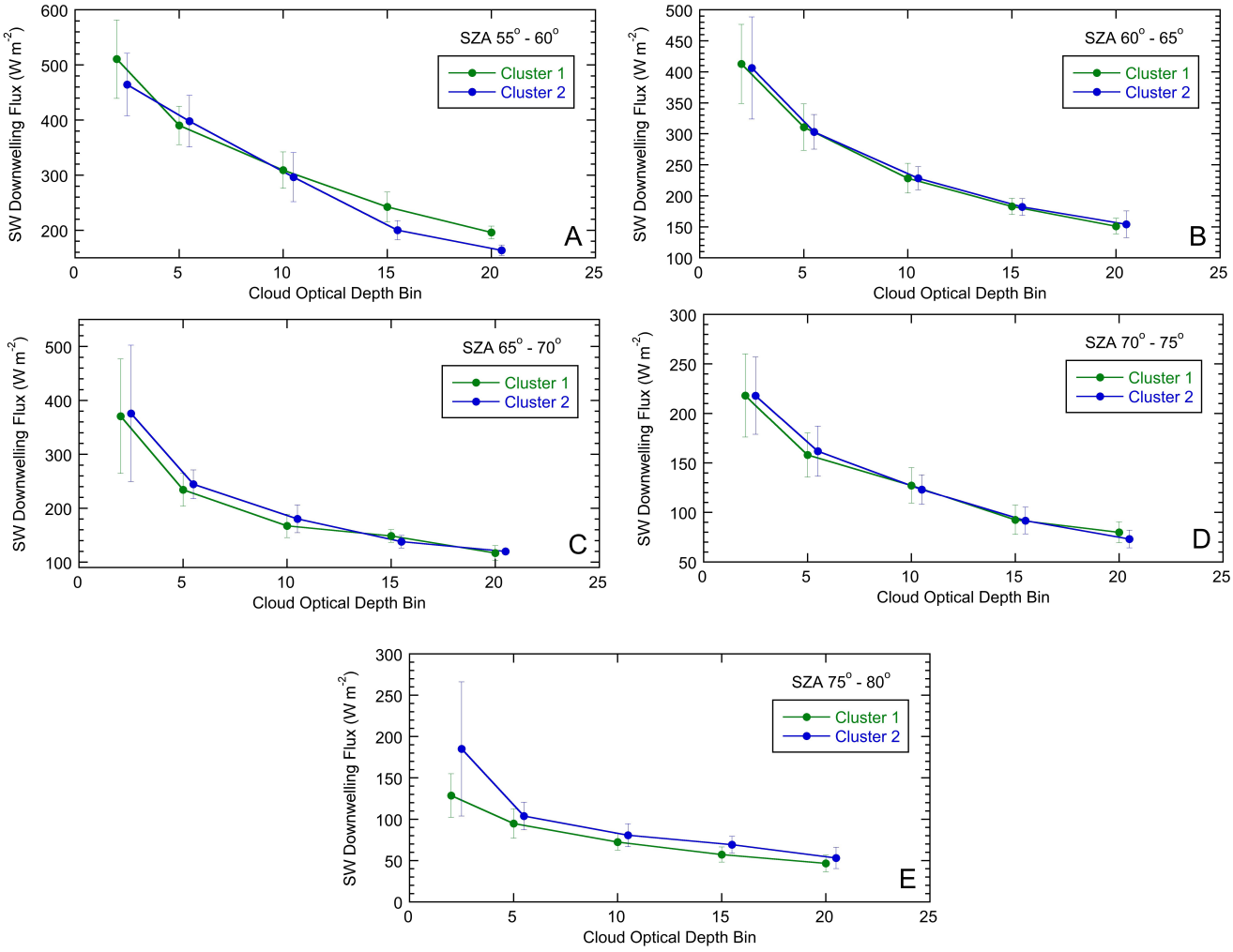

Figure 13: Plots showing the downwelling SW flux as a function of cloud optical depth bins, comparing the SW flux of Regime 1 (green) and Regime 2 (blue). Each plot represents a different SZA range.

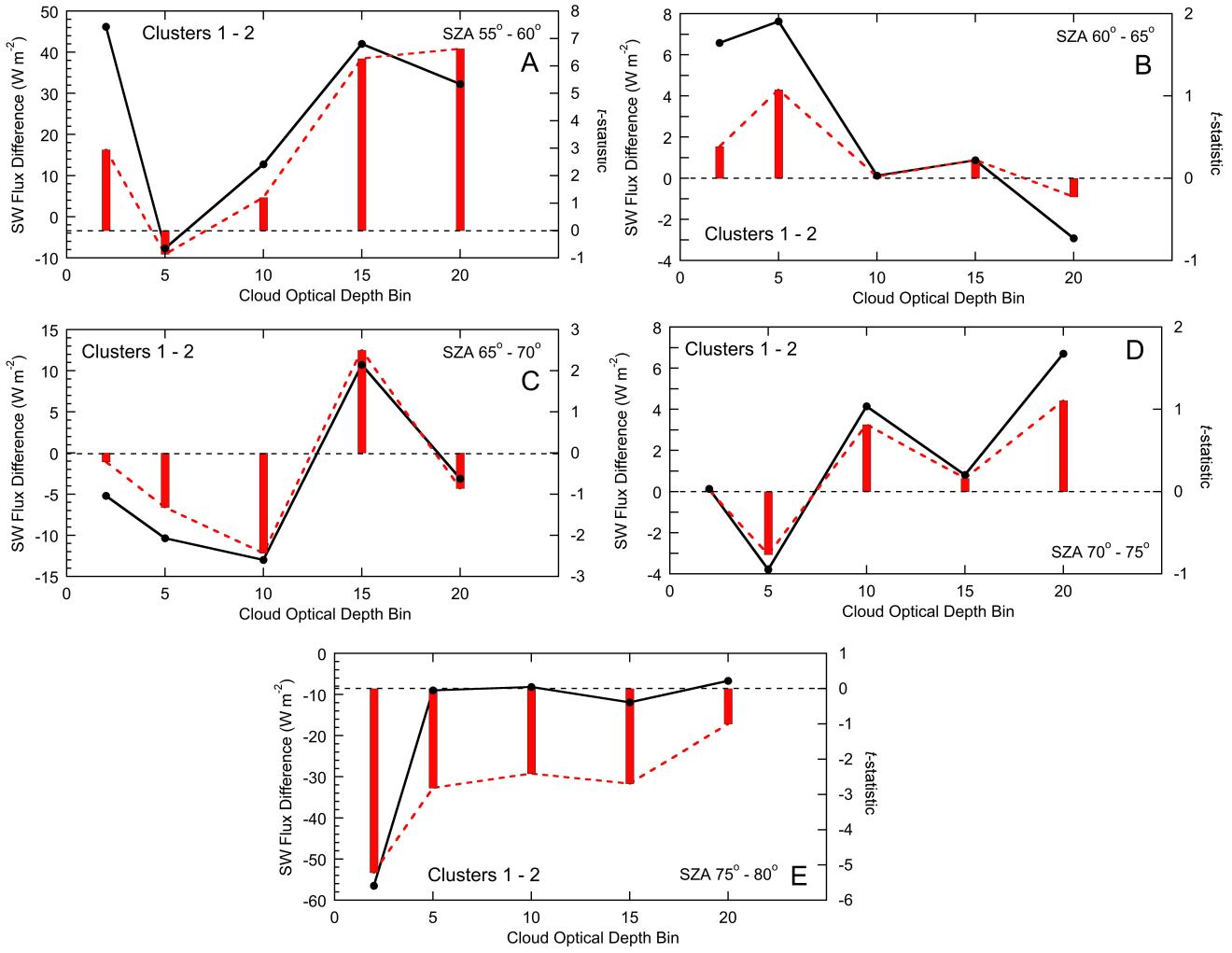

Figure 14: Plots depicting the difference in downwelling SW flux from Regime 1 to Regime 2, as a function of cloud optical depth bins and varying SZA ranges. The t-Statistic is plotted as vertical red bars.

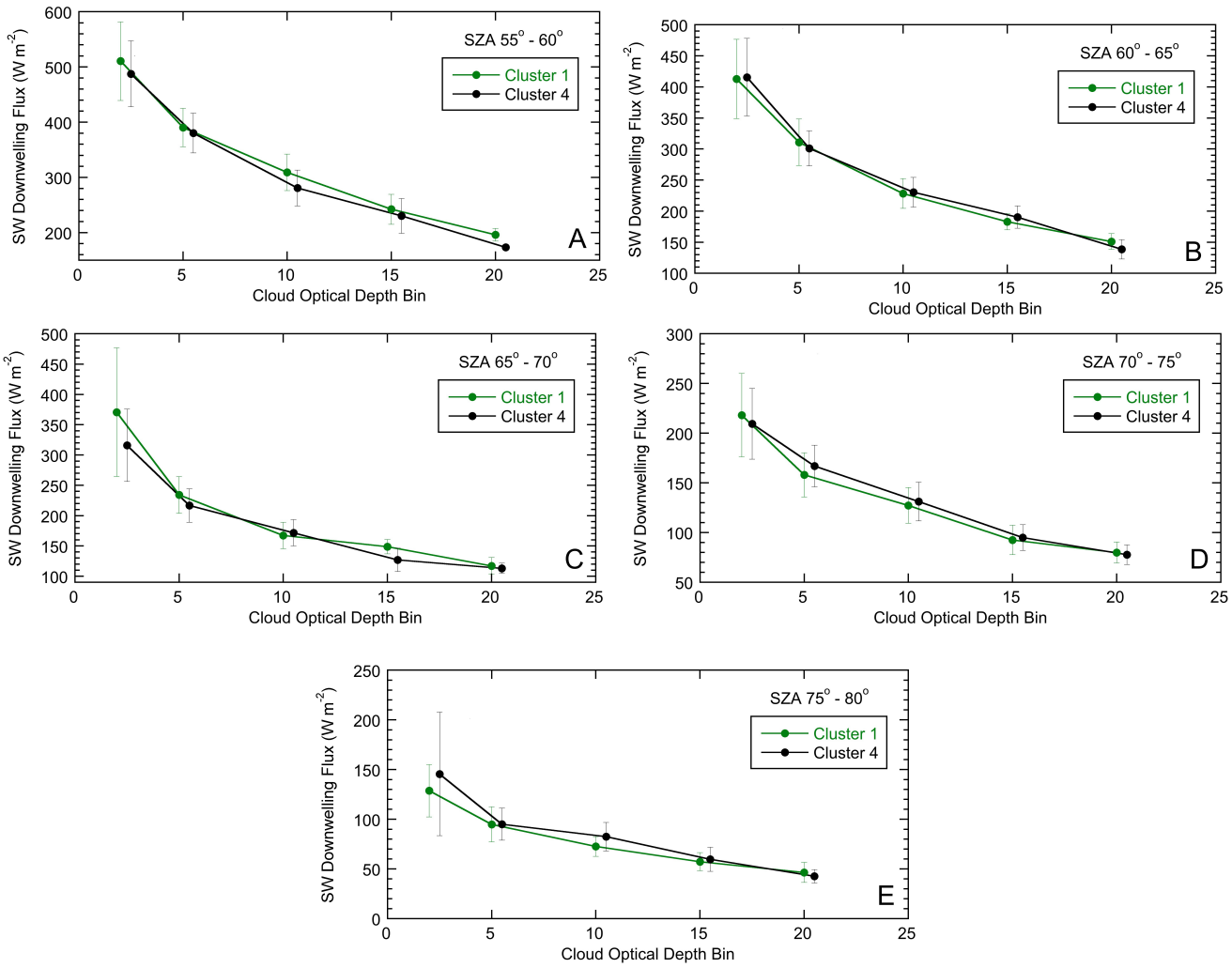

Figure 15: Plots showing the downwelling SW flux as a function of cloud optical depth bins, comparing the SW flux of Regime 1 (green) and Regime 4 (black). Each plot represents a different SZA range.

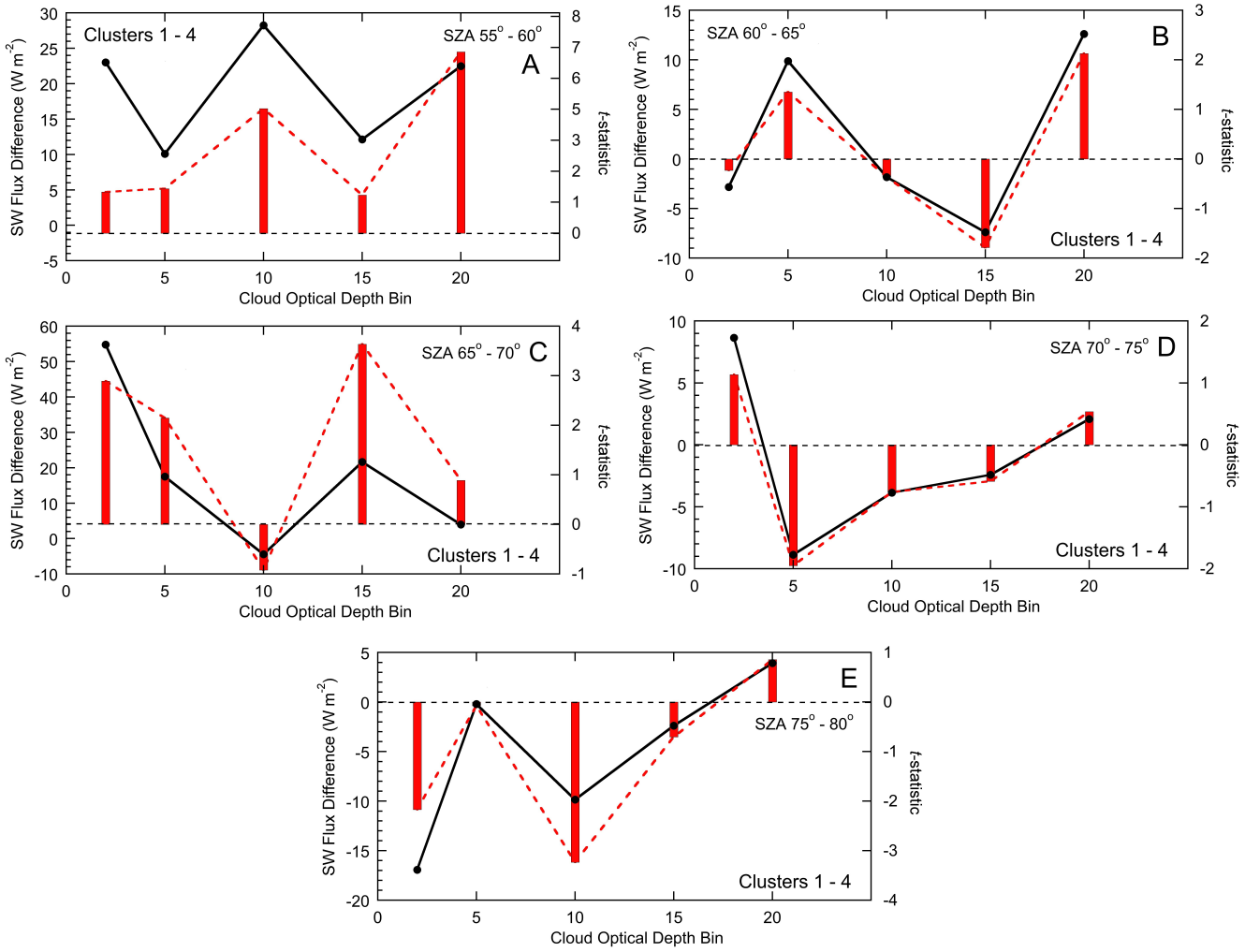

Figure 16: Plots depicting the difference in downwelling SW flux from Regime 1 to Regime 4, as a function of cloud optical depth bins and varying SZA ranges. The t-Statistic is plotted as vertical red bars.

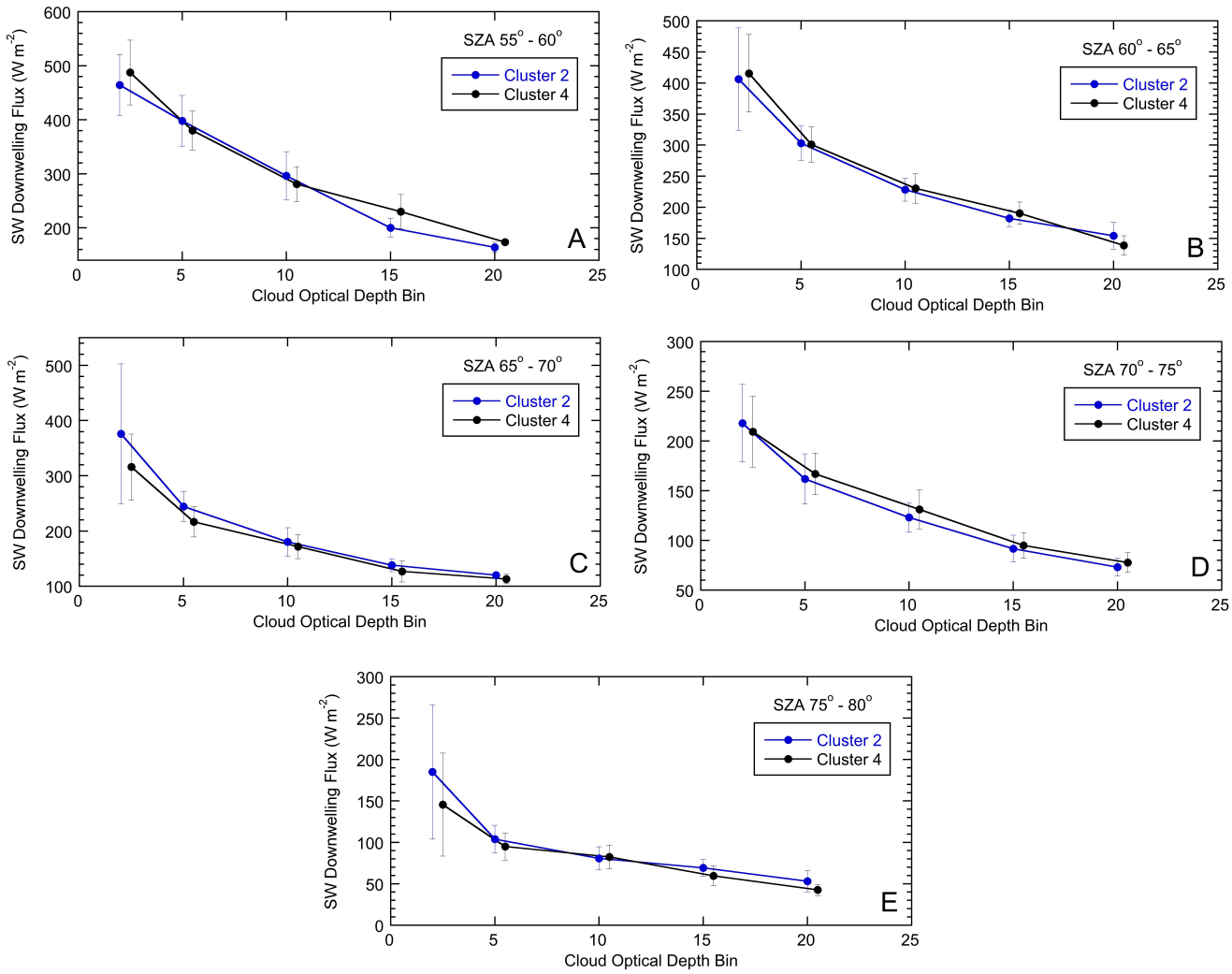

Figure 17: Plots showing the downwelling SW flux as a function of cloud optical depth bins, comparing the SW flux of Regime 2 (blue) and Regime 4 (black). Each plot represents a different SZA range.

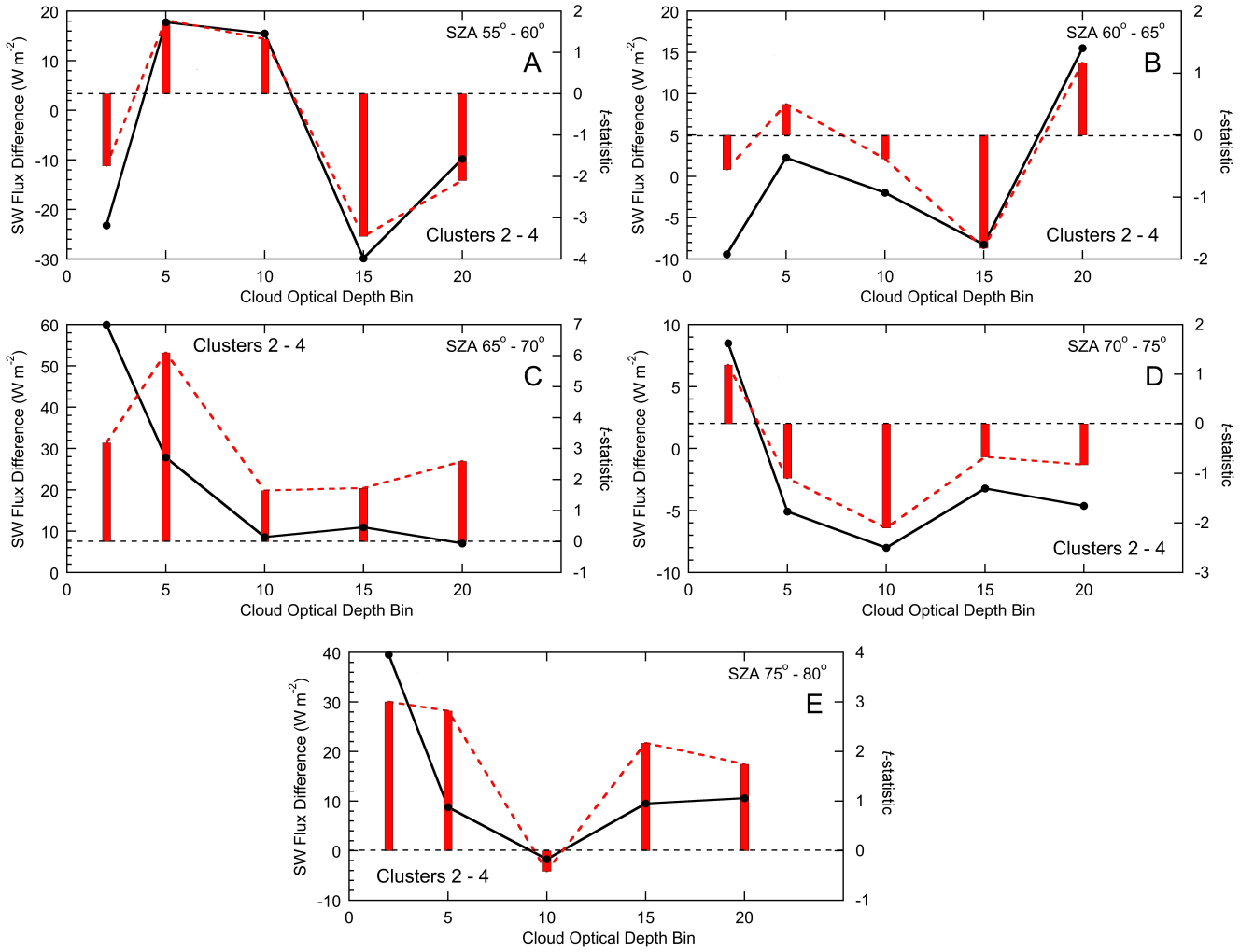

Figure 18: Plots depicting the difference in downwelling SW flux from Regime 2 to Regime 4, as a function of cloud optical depth bins and varying SZA ranges. The t-Statistic is plotted as vertical red bars.

Shortwave τ Comparison

Comparing all Solar Zenith Angles and Cloud Optical Depth Bins -
Tabulate fraction of bins that have positive difference between two regimes

Regime Pairing	Bins			Student's t-Test
	Number of Bins (N)	N Difference > 0	%	N (Statistically Significant Bins)
Regime 1 & 2	25	13	52	4
Regime 1 & 4	25	14	56	6
Regime 2 & 4	25	14	56	5

Figure 19: Regime Shortwave ??Differences Summary Results

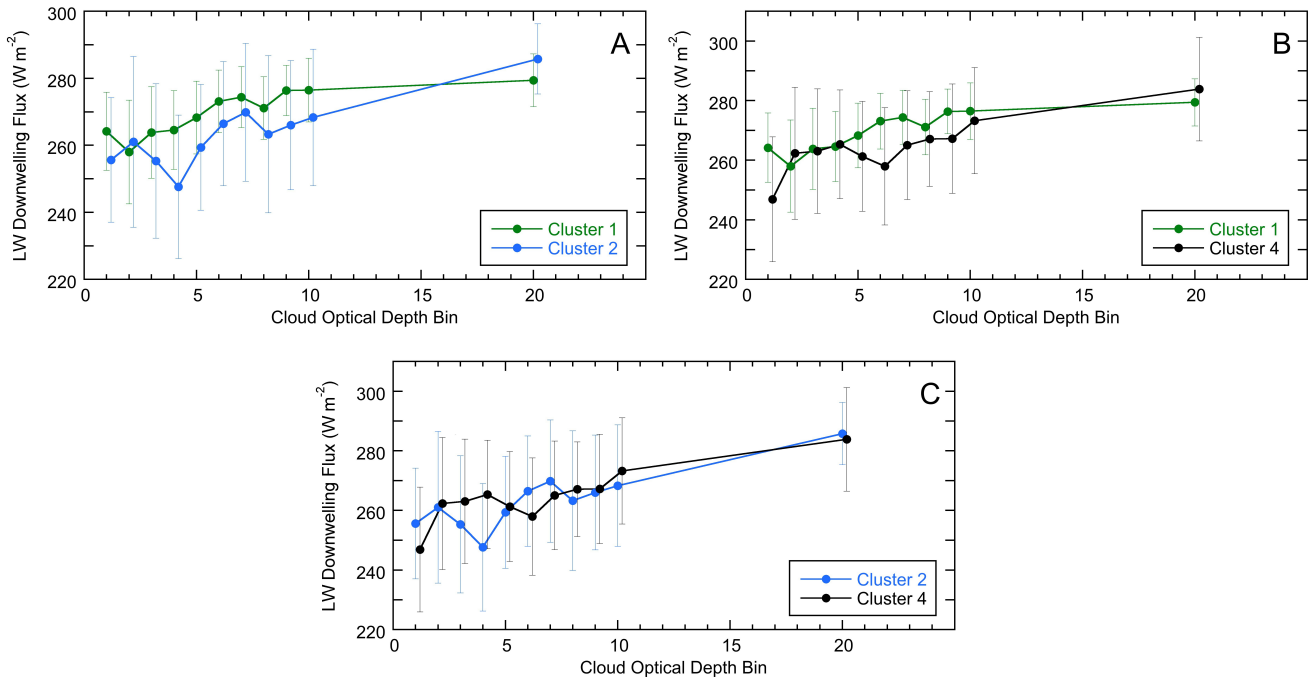

Figure 20: Plots showing the downwelling LW flux as a function of cloud optical depth bins, with each regime pairing represented.

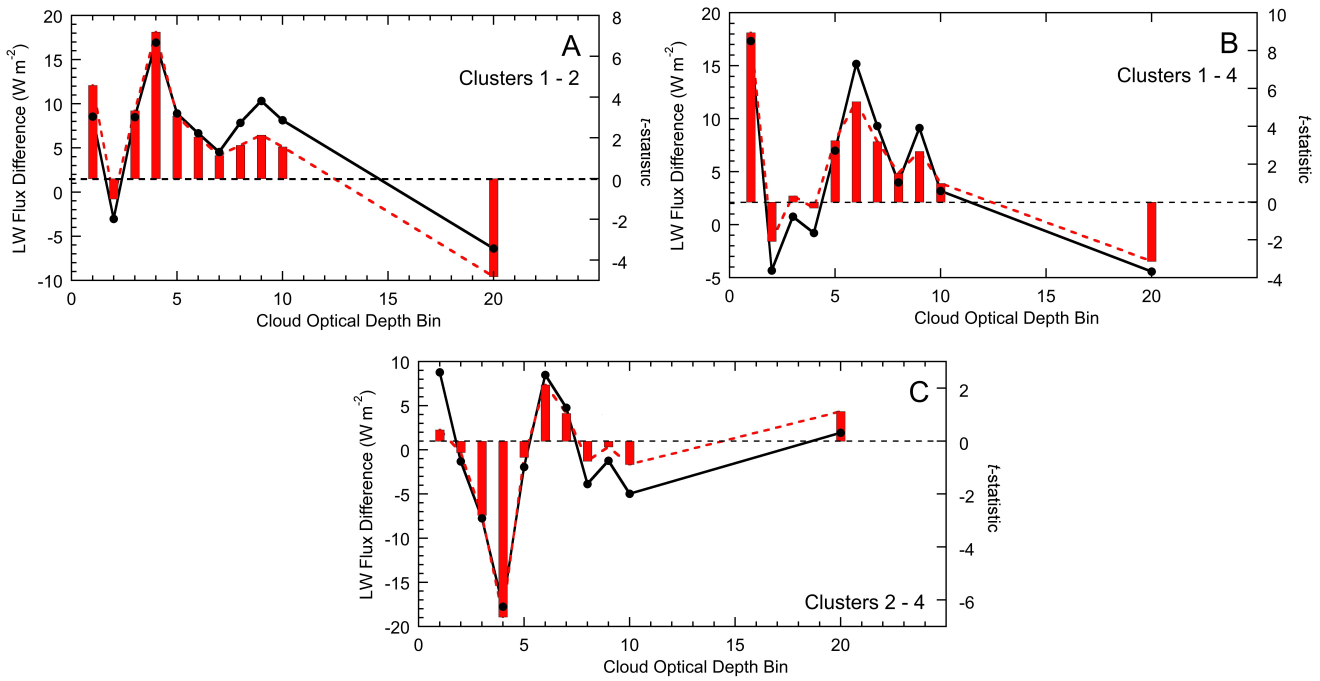

Figure 21: Plots depicting the difference in downwelling LW flux for each regime-cluster pairing, as a function of cloud optical depth bins. The t-Statistic is plotted as vertical red bars.

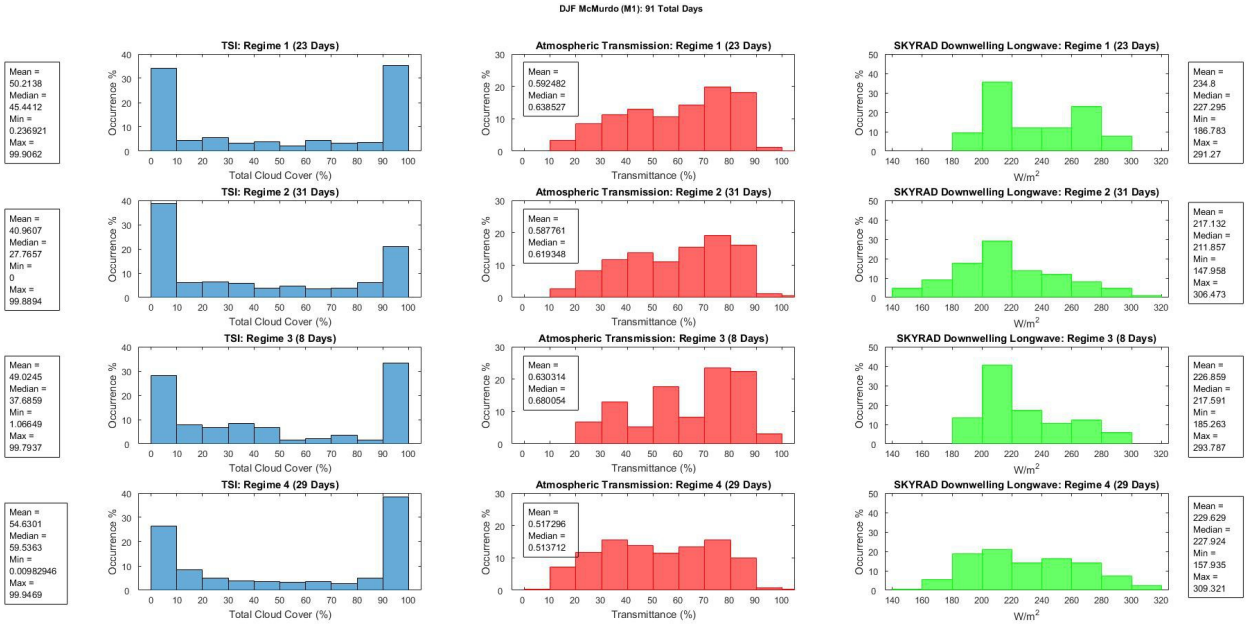

Figure 22: Multiple regime-sorted histograms (percentage of occurrence) for TSI Total Percent Cloud Cover (Blue), SKYRAD Broadband Shortwave Atmospheric Transmission (Red), and SKYRAD Broadband Downwelling Longwave (Green).

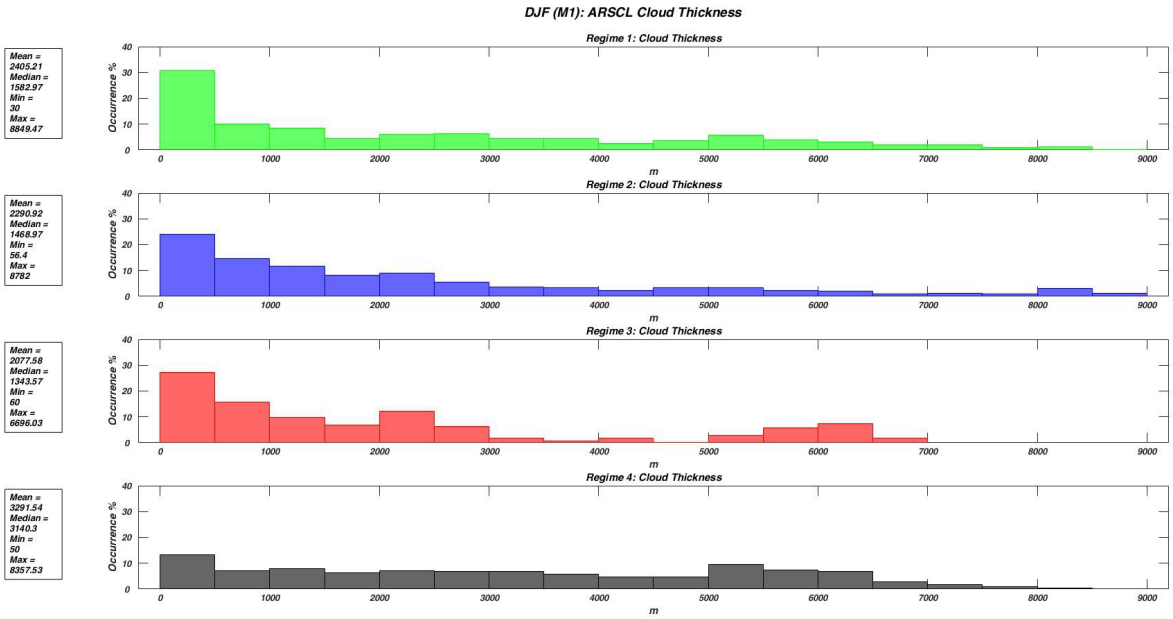

Figure 23: Regime-sorted histograms (percentage of occurrence) for ARSCL calculated cloud thickness.

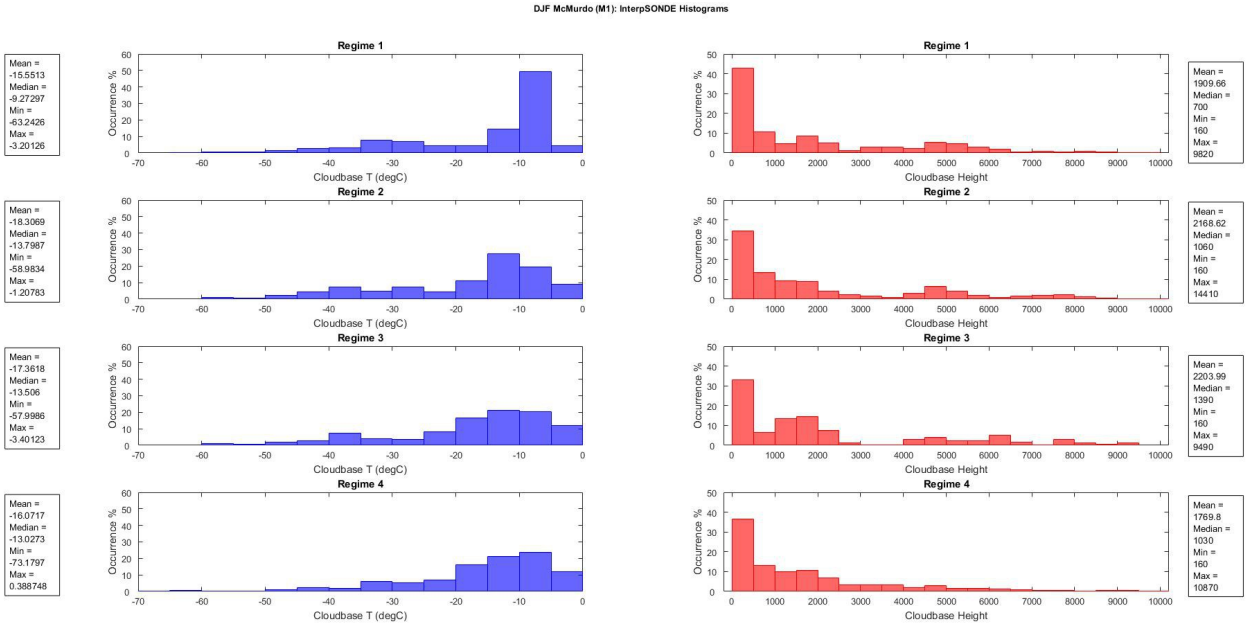

Figure 24: Multiple regime-sorted histograms (percentage of occurrence) for ARSCL/INTERPSONDE calculated cloud base temperature (blue) and ARSCL cloud base height (red).

References

AMRC AWS Data Form. http://amrc.ssec.wisc.edu/aws/api/form.html (Accessed April 30, 2018).

Atmospheric Radiation Measurement (ARM) Climate Research Facility. 1996, updated hourly. Ground Radiometers on Stand for Upwelling Radiation (GNDRAD60S). 2015-12-01 to 2016-02-29, ARM Mobile Facility (AWR) McMurdo Station Ross Ice Shelf, Antarctica; AMF2 (M1). Compiled by A. Andreas, A. Habte, I. Reda, M. Dooraghi, M. Kutchenreiter, M. Sengupta, V. Morris and Y. Xie. Atmospheric Radiation Measurement (ARM) Climate Research Facility Data Archive: Oak Ridge, Tennessee, USA. Data set accessed 2016-09-01 at http://dx.doi.org/10.5439/1025192.

Atmospheric Radiation Measurement (ARM) Climate Research Facility. 1990, updated hourly. Multifilter Radiometer (MFR). 2015-12-01 to 2016-02-29, ARM Mobile Facility (AWR) McMurdo Station Ross Ice Shelf, Antarctica; AMF2 (M1). Compiled by A. Mendoza, B. Ermold, C. Flynn, C. Herrera, C. Long, G. Hodges, K. Gaustad, L. Ma, L. Riihimaki, Q. Min, R. Wagener, V. Morris and Y. Shi. Atmospheric Radiation Measurement (ARM) Climate Research Facility Data Archive: Oak Ridge, Tennessee, USA. Data set accessed 2016-09-01 at http://dx.doi.org/10.5439/1023898.

Atmospheric Radiation Measurement (ARM) Climate Research Facility. 1990, updated hourly. Multifilter Rotating Shadowband Radiometer (MFRSR). 2015-12-01 to 2016-02-29, ARM Mobile Facility (AWR) McMurdo Station Ross Ice Shelf, Antarctica; AMF2 (M1). Compiled by B. Ermold, C. Flynn, C. Herrera, C. Long, G. Hodges, K. Gaustad, L. Ma, L. Riihimaki, Q. Min, R. Wagener and Y. Shi. Atmospheric Radiation Measurement (ARM) Climate Research Facility Data Archive: Oak Ridge, Tennessee, USA. Data set accessed 2016-09-01 at http://dx.doi.org/10.5439/1023898.

Atmospheric Radiation Measurement (ARM) Climate Research Facility. 1996, updated hourly. Sky Radiometers on Stand for Downwelling Radiation (SKYRAD20S). 2015-12-01 to 2016-02-29, ARM Mobile Facility (AWR) McMurdo Station Ross Ice Shelf, Antarctica; AMF2 (M1). Compiled by A. Andreas, A. Habte, I. Reda, K. Gaustad, L. Riihimaki, M. Dooraghi, M. Kutchenreiter, M. Sengupta, V. Morris and Y. Xie. Atmospheric Radiation Measurement (ARM) Climate Research Facility Data Archive: Oak Ridge, Tennessee, USA. Data set accessed 2016-09-02 at http://dx.doi.org/10.5439/1025280.

Atmospheric Radiation Measurement (ARM) Climate Research Facility. 1993, updated hourly. Balloon-Borne Sounding System (SONDEWRPR). 2015-12-01 to 2016-02-29, ARM Mobile Facility (AWR) McMurdo Station Ross Ice Shelf, Antarctica; AMF2 (M1). Compiled by C. Sivaraman, D. Holdridge, D. Troyan, J. Kyrouac, L. Riihimaki, R. Coulter, S. Giangrande, T. Shippert and T. Toto. Atmospheric Radiation Measurement (ARM) Climate Research Facility Data Archive: Oak Ridge, Tennessee, USA. Data set accessed 2016-09-02 at http://dx.doi.org/10.5439/1150271.

Atmospheric Radiation Measurement (ARM) Climate Research Facility. 1994, updated hourly. Total Sky Imager (TSISKYCOVER). 2015-12-01 to 2016-02-29, ARM Mobile Facility (AWR) McMurdo Station Ross Ice Shelf, Antarctica; AMF2 (M1). Compiled by B. Holben, C. Flynn, L. Gregory, L. Ma, R. Wagener and V. Morris. Atmospheric Radiation Measurement (ARM) Climate Research Facility Data Archive: Oak Ridge, Tennessee, USA. Data set accessed 2016-09-02 at http://dx.doi.org/10.5439/1025308.

Atwater, M. A., and J. T. Ball, 1981: A Surface Solar Radiation Model for Cloudy Atmospheres. *Monthly Weather Review*, **109**, 878–888, doi:10.1175/1520-0493(1981)109<0878:assrmf>2.0.co;2.

Bintanja, R., and M. R. V. D. Broeke, 1996: The Influence Of Clouds On The Radiation Budget Of Ice And Snow Surfaces In Antartica And Greenland In Summer. *International Journal of Climatology*, **16**, 1281–1296, doi:10.1002/(sici)1097-0088(199611)16:11<1281::aid-joc83>3.3.co;2-1.

Bretherton, C. S., M. Widmann, V. P. Dymnikov, J. M. Wallace, and I. Bladé, 1999: The Effective Number of Spatial Degrees of Freedom of a Time-Varying Field. *Journal of Climate*, **12**, 1990–2009, doi:10.1175/1520-0442(1999)012<1990:tenosd>2.0.co;2.

David H. Bromwich, Julien P. Nicolas, Keith M. Hines, Jennifer E. Kay, Erica L. Key, Matthew A. Lazzara, Dan Lubin, Greg M. McFarquhar, Irina V. Gorodetskaya, Daniel P. Grosvenor, Thomas Lachlan-Cope, Nicole P. M. van Lipzig, 2012: Tropospheric clouds in Antarctica. *Reviews of Geophysics*, **50**, doi:10.1029/2011rg000363.

Cess, R. D., T. Qian, and M. Sun, 2000: Consistency tests applied to the measurement of total, direct, and diffuse shortwave radiation at the surface. *Journal of Geophysical Research: Atmospheres*, **105**, 24881–24887, doi:10.1029/2000jd900402.

Eugene E. Clothiaux, Mark A. Miller, Robin C. Perez, David D. Turner, Kenneth P. Moran, Brooks E. Martner, Thomas P. Ackerman, Gerald G. Mace, Roger T. Marchand, Kevin B. Widener, Daniel J. Rodriguez, Taneil Uttal, James H. Mather, Connor J. Flynn, Krista L. Gaustad, Brian Ermold, 2001: *The ARM Millimeter Wave Cloud Radars (MMCRs) and the Active Remote Sensing of Clouds (ARSCL) value added product (VAP)*. Pacific Northwest National Laboratory, Richland, WA.

Clothiaux, E. E., M. A. Miller, B. A. Albrecht, T. P. Ackerman, J. Verlinde, D. M. Babb, R. M. Peters, and W. J. Syrett, 1995: An Evaluation of a 94-GHz Radar for Remote Sensing of Cloud Properties. *Journal of Atmospheric and Oceanic Technology*, **12**, 201–229, doi:10.1175/1520-0426(1995)012<0201:aeoagr>2.0.co;2.

Clothiaux, E. E., G. G. Mace, T. P. Ackerman, T. J. Kane, J. D. Spinhirne, and V. S. Scott, 1998: An Automated Algorithm for Detection of Hydrometeor Returns in Micropulse Lidar Data. *Journal of Atmospheric and Oceanic Technology*, **15**, 1035–1042, doi:10.1175/1520-0426(1998)015<1035:aaafdo>2.0.co;2.

Clothiaux, Eugene E., Moran, Kenneth P., Martner, Brooks E., Ackerman, Thomas P., Mace, Gerald G., Uttal, Taneil, Mather, James H., Widener, Kevin B., Miller, Mark A., Rodriguez, Daniel J., 1999: The Atmospheric Radiation Measurement Program Cloud Radars: Operational Modes. *Journal of Atmospheric and Oceanic Technology*, **16**, 819–827, doi:10.1175/1520-0426(1999)016<0819:tarmpc>2.0.co;2.

Coulson, K. L., 1975: Terrestrial Radiation: Methods of Measurement. *Solar and Terrestrial Radiation*, 279–307, doi:10.1016/b978-0-12-192950-3.50015-2.

Fitzpatrick, M. F., R. E. Brandt, and S. G. Warren, 2004: Transmission of Solar Radiation by Clouds over Snow and Ice Surfaces: A Parameterization in Terms of Optical Depth, Solar Zenith Angle, and Surface Albedo. *Journal of Climate*, **17**, 266–275, doi:10.1175/1520-0442(2004)017<0266:tosrbc>2.0.co;2.

Fitzpatrick, M. F., and S. G. Warren, 2005: Transmission of Solar Radiation by Clouds over Snow and Ice Surfaces. Part II: Cloud Optical Depth and Shortwave Radiative Forcing from Pyranometer Measurements in the Southern Ocean. *Journal of Climate*, **18**, 4637–4648, doi:10.1175/jcli3562.1.

Fitzpatrick, M. F., and S. G. Warren, 2007: The Relative Importance of Clouds and Sea Ice for the Solar Energy Budget of the Southern Ocean. *Journal of Climate*, **20**, 941–954, doi:10.1175/jcli4040.1.

Fogt, R. L., and D. H. Bromwich (2008), Atmospheric moisture and cloud cover characteristics forecast by AMPS, *Weather Forecasting*, **23**, 914–930, doi:10.1175/2008WAF2006100.1.

Harrison, L., J. Michalsky, and J. Berndt, 1994: Automated multifilter rotating shadow-band radiometer: an instrument for optical depth and radiation measurements. *Applied Optics*, **33**, 5118, doi:10.1364/ao.33.005118.

Harrison, L., and J. Michalsky, 1994: Objective algorithms for the retrieval of optical depths from ground-based measurements. *Applied Optics*, **33**, 5126, doi:10.1364/ao.33.005126.

Jensen, M. P., and T. Toto, 2016: Interpolated Sounding and Gridded Sounding Value-Added Products. doi:10.2172/1326751.

Johnson, N. C., and S. B. Feldstein, 2010: The Continuum of North Pacific Sea Level Pressure Patterns: Intraseasonal, Interannual, and Interdecadal Variability. *Journal of Climate*, **23**, 851–867, doi:10.1175/2009jcli3099.1.

Kassianov, E., C. N. Long, and M. Ovtchinnikov, 2005: Cloud Sky Cover versus Cloud Fraction: Whole-Sky Simulations and Observations. *Journal of Applied Meteorology*, **44**, 86–98, doi:10.1175/jam-2184.1.

Robert E. Kopp, Andrew C. Kemp, Klaus Bittermann, Benjamin P. Horton, Jeffrey P. Donnelly, W. Roland Gehrels, Carling C. Hay, Jerry X. Mitrovica, Eric D. Morrow, and Stefan Rahmstorf, 2016: Temperature-driven global sea level variability in the Common Era. *Proc. Natl. Acad. Sci. USA*, **113**, E1434–E1441, doi:10.1073/pnas.1517056113.

Lazzara, Matthew. "The University of Wisconsin-Madison Antarctic Meteorology Program." Meteorological Technology International January 2010: 88. Print.

Lefebvre, W., 2004: Influence of the Southern Annular Mode on the sea ice–ocean system. *Journal of Geophysical Research*, **109**, doi:10.1029/2004jc002403.

Lesht, BM. 1995. “An Evaluation of ARM Radiosonde Operational Performance.” Proceedings of the Ninth Symposium on Meteorological Observations and Instrumentation, pp. 6–10. *American Meteorological Society*, Boston, Massachusetts.

Long, C., D. Slater, and T. Tooman, 2001: Total Sky Imager Model 880 Status and Testing Results. doi:10.2172/1020735.

Lubin, D., and A. M. Vogelmann, 2011: The influence of mixed-phase clouds on surface shortwave irradiance during the Arctic spring, *Journal of Geophysical Research*, **116**, doi:10.1029/2011JD015761.

Lubin D, J Verlinde, DH Bromwich, AM Vogelmann, and LM Russell. 2015. ARM West Antarctic Radiation Experiment (AWARE) Science Plan. Ed. by Robert Stafford, DOE ARM Climate Research Facility. DOE/SC-ARM-15-040.

Lubin D, DH Bromwich, AM Vogelmann, J Verlinde, and LM Russell. 2017. ARM West Antarctic Radiation Experiment (AWARE) Field Campaign Report. Ed. by Robert Stafford, ARM Research Facility. DOE/SC-ARM-17-028.

MathWorks – Support. *MathWorks - Support - MATLAB & Simulink*. https://www.mathworks.com/support.html?s_tid=gn_supp (Accessed April 30, 2018).

Monaghan, A. J., D. H. Bromwich, J. G. Powers, and K. W. Manning (2005), The climate of the McMurdo, Antarctica, region as represented by one year of forecasts from the Antarctic mesoscale prediction system, *J. Clim*., **18**, 1174–1189, doi:10.1175/JCLI3336.1.

Mülmenstädt, J., D. Lubin, L. M. Russell, and A. M. Vogelmann, 2012: Cloud Properties over the North Slope of Alaska: Identifying the Prevailing Meteorological Regimes. *Journal of Climate*, **25**, 8238–8258, doi:10.1175/jcli-d-11-00636.1.

Nicolas, J. P., and D. H. Bromwich, 2011: Climate of West Antarctica and Influence of Marine Air Intrusions*. *Journal of Climate*, **24**, 49–67, doi:10.1175/2010jcli3522.1.

Julien P. Nicolas, Andrew M. Vogelmann, Ryan C. Scott, Aaron B. Wilson, Maria P. Cadeddu, David H. Bromwich, Johannes Verlinde, Dan Lubin, Lynn M. Russell, Colin Jenkinson, Heath H. Powers, Maciej Ryczek, Gregory Stone & Jonathan D. Wille, 2017: January 2016 extensive summer melt in West Antarctica favoured by strong El Niño. *Nat. Commun.*, **8**, 15799, doi:10.1038/ncomms15799.

Nigro, M. A., and J. J. Cassano, 2014: Identification of Surface Wind Patterns over the Ross Ice Shelf, Antarctica, Using Self-Organizing Maps. *Monthly Weather Review*, **142**, 2361–2378, doi:10.1175/mwr-d-13-00382.1.

Nigro, M. A., and J. J. Cassano, 2014: Analysis of the Ross Ice Shelf Airstream Forcing Mechanisms Using Self-Organizing Maps. *Monthly Weather Review*, **142**, 4719–4734, doi:10.1175/mwr-d-14-00077.1.

Parish, T. R., J. J. Cassano, and M. W. Seefeldt, 2006: Characteristics of the Ross Ice Shelf air stream as depicted in Antarctic Mesoscale Prediction System simulations. *Journal of Geophysical Research*, **111**, doi:10.1029/2005jd006185.

Record-breaking La Niña events. *The 2010–11 and 2011–12 La Niña events in Australia*. http://www.bom.gov.au/climate/enso/history/ln-2010-12/ (Accessed April 30, 2018).

Roeder L. 2015. ARM West Antarctic Radiation Experiment (AWARE) Backgrounder. Ed. by Dana DuPont, ARM Climate Research Facility. DOE/SC-ARM-15-045.

Scott, R. C., and D. Lubin, 2014: Mixed-phase cloud radiative properties over Ross Island, Antarctica: The influence of various synoptic-scale atmospheric circulation regimes. *Journal of Geophysical Research: Atmospheres*, **119**, 6702–6723, doi:10.1002/2013jd021132.

Scott, R. C., and D. Lubin, 2016: Unique manifestations of mixed-phase cloud microphysics over Ross Island and the Ross Ice Shelf, Antarctica. *Geophysical Research Letters*, **43**, 2936–2945, doi:10.1002/2015gl067246.

Scott, R. C., D. Lubin, A. M. Vogelmann, and S. Kato, 2017: West Antarctic Ice Sheet Cloud Cover and Surface Radiation Budget from NASA A-Train Satellites. *Journal of Climate*, **30**, 6151–6170, doi:10.1175/jcli-d-16-0644.1.

Scott, R. C., J. P. Nicolas, D. H. Bromwich, J. R. Norris, and D. Lubin (2018) Meteorological Drivers and Large-Scale Climate Forcing of West Antarctic Surface Melt, *Journal of Climate.*

Scott, R. C., C. Glennon, D. Lubin, A. M. Vogelmann, S. H. Wang, D. H. Bromwich, J. Verlinde, and L. M. Russell (2018), Influence of Meteorological Regimes on Cloud Properties over Ross Island, Antarctica: A User's Guide to AWARE Data.

Andrew Shepherd, Erik R. Ivins, Geruo A, Valentina R. Barletta, Mike J. Bentley, Srinivas Bettadpur, Kate H. Briggs, 2012: A reconciled estimate of icesheet mass balance. *Science*, **338**, 1183–1189, doi:10.1126/science.1228102.

Shupe, M. D., S. Y. Matrosov, and T. Uttal, 2006: Arctic Mixed-Phase Cloud Properties Derived from Surface-Based Sensors at SHEBA. *Journal of the Atmospheric Sciences*, **63**, 697–711, doi:10.1175/jas3659.1.

Solar Position Calculator. http://www.instesre.org/Aerosols/sol_calc.htm (Accessed April 30, 2018).

Steinhoff, D. F., S. Chaudhuri, and D. H. Bromwich, 2009: A Case Study of a Ross Ice Shelf Airstream Event: A New Perspective*. *Monthly Weather Review*, **137**, 4030–4046, doi:10.1175/2009mwr2880.1.

Stierle, S., *Solar Geom Calc*. https://www.esrl.noaa.gov/gmd/grad/antuv/SolarCalc.jsp (Accessed April 30, 2018).

Trevino, A., Introduction to K-means Clustering. *DataScience.com*. https://www.datascience.com/blog/k-means-clustering (Accessed April 30, 2018).

Tsukernik, M., and A. H. Lynch (2013), Atmospheric meridional moisture flux over the Southern Ocean: A story of the Amundsen Sea, *J. Clim.*, **26**, 8055–8064, doi:10.1175/JCLI-D-12-00381.1.

Turner, D. D., S. A. Clough, J. C. Liljegren, E. E. Clothiaux, K. E. Cady-Pereira, and K. L. Gaustad, 2007: Retrieving Liquid Wat0er Path and Precipitable Water Vapor From the Atmospheric Radiation Measurement (ARM) Microwave Radiometers. *IEEE Transactions on Geoscience and Remote Sensing*, **45**, 3680–3690, doi:10.1109/tgrs.2007.903703.

Uttal, T., S. Y. Matrosov, J. B. Snider, and R. A. Kropfli, 1994: Relationship between Ice Water Path and Downward Longwave Radiation for Clouds Optically Thin in the Infrared: Observations and Model Calculations. *Journal of Applied Meteorology*, **33**, 348–357, doi:10.1175/1520-0450(1994)033<0348:rbiwpa>2.0.co;2.

K. Van Tricht, S. Lhermitte, J. T. M. Lenaerts, I. V. Gorodetskaya, T. S. L'Ecuyer, B. Noël, M. R. van den Broeke, D. D. Turner & N. P. M. van Lipzig, 2016: Clouds enhance Greenland ice sheet meltwater runoff. *Nat. Commun*., **7**, 10266, doi:10.1038/ncomms10266.

Vaughan, D. G., G. J. Marshall, W. M. Connolley, C. Parkinson, R. Mulvaney, D. A. Hodgson, J. C. King, C. J. Pudsey, and J. Turner (2003), Recent rapid regional climate warming on the Antarctic Peninsula, *Clim*. *Change*, **60**, 243–274, doi:10.1023/%3A1026021217991.

Zwally, H. J.,W. Abdalati, T. Herring, K. Larson, J. Saba, and K. Steffen, 2002: Surface melt-induced acceleration of Greenland ice-sheet flow. *Science*, **297**, 218–222, doi:10.1126/science.1072708.